An Application of Linear Covariance Analysis to the Design of Responsive Near-Rendezvous Missions

by

Benjamin Lee Visser

B.S. Astronautical Engineering
United States Air Force Academy, 2005

SUBMITTED TO THE DEPARTMENT OF AERONAUTICS AND ASTRONAUTICS
IN PARTIAL FULFILLMENT OF THE REQUIREMENTS FOR THE DEGREE OF

MASTER OF SCIENCE IN AERONAUTICS AND ASTRONAUTICS
AT THE
MASSACHUSETTS INSTITUTE OF TECHNOLOGY

JUNE 2007

Author:_____
Department of Aeronautics and Astronautics
May 25, 2007

Certified by:_____
Dr. Piero Miotto
Member of the Technical Staff, Charles Stark Draper Laboratory
Thesis Supervisor

Certified by:_____
Dr. George T. Schmidt
Lecturer, Department of Aeronautics and Astronautics
Thesis Advisor

Accepted by:_____
Jaime Peraire
Professor, Department of Aeronautics and Astronautics
Chair, Committee on Graduate Students

[This page intentionally left blank.]

An Application of Linear Covariance Analysis to the Design of Responsive Near-Rendezvous Missions

by

Benjamin Lee Visser

Submitted to the Department of Aeronautics and Astronautics
on May 25, 2007, in partial fulfillment of the
requirements for the degree of
Master of Science in Aeronautics and Astronautics

Abstract

This thesis investigates a new class of launch vehicles capable of being released from an aircraft which ultimately have the goal of achieving near-rendezvous conditions at orbital altitudes up to 800 *km*. These launch vehicles would be capable of carrying small payloads, on the order of two to six kilograms, and would be much more responsive to a customer's needs than the current space launch infrastructure, in which it may take months of preparation for a launch.

To fully describe the mission in this thesis, it is broken up into three phases: atmospheric launch, orbit raising, and near-rendezvous operations. An analysis method known as Linear Covariance analysis is introduced to provide a platform of estimating the navigation covariance and dispersion of the spacecraft during the second and third phases, while the first phase, up to main-engine-cutoff, is examined using a three degree-of-freedom simulation.

The goal of this thesis is to demonstrate the utility of Linear Covariance analysis to responsive space mission planning. This is accomplished by first explaining the mathematics that underlie the method. Next the software used for the analysis, Lincov Tools, is explained in detail, the mission is examined more closely, and the hardware for both the payload and launch vehicle are briefly discussed. Finally, the combination of the three degree-of-freedom simulation and Lincov Tools are employed to the space mission and the results are presented.

Thesis Supervisor: Dr. Piero Miotto
Title: Member of the Technical Staff, Charles Stark Draper Laboratory

Thesis Advisor: Dr. George T. Schmidt
Title: Lecturer, Department of Aeronautics and Astronautics

[This page intentionally left blank.]

Acknowledgments

First, I would like to thank my supervisor, Piero Miotto of Draper Laboratory, for his incredible patience, sound technical support, and encouragement during my two year course of study at MIT. Without him I would have never found my way through completion. Also, my sincere thanks go to George Schmidt for agreeing to step in at the last minute to help me complete my degree. In addition, I thank David Benson for providing encouragement during the final stages of this thesis. Many other members of Draper Laboratory provided technical support and feedback, including Greg Andrews, Tony Kourepenis, Brad Moran, Ernie Griffith, Pete Sherman, and Nate Lowry.

Over the course of the program I had the pleasure of working with a few other fine engineers not employed at Draper Laboratory, who contributed to this thesis in one way or another. They included David Gonzales, George Haldeman and Tony Hotz of MIT Lincoln Laboratory, Adam London of Ventions LLC, John Sheehan of Lockheed Martin, professor Alan Epstein and then professor James Paduano of MIT, and finally Fred Kennedy of DARPA.

I would also like to acknowledge my previous institution, the United States Air Force Academy, primarily the Department of Astronautical Engineering, for providing the opportunities, outstanding educational experience, and mentorship that helped me reach this point. In particular I would like to thank the following past instructors of mine: Tim Lawrence, Dan Miller, Ronald Lisowski, and Scott Dahlke.

Lastly, I would like to thank the United States Air Force for allowing me to spend two years at MIT as an active-duty officer in pursuit of a graduate degree. In addition I owe a debt of gratitude to The Charles Stark Draper Laboratory for providing the means necessary for this study to take place. To my fellow USAFA graduates, friends at MIT and Raymond Street, my family and friends back home, and especially my girlfriend, thank you very much for believing in me and encouraging me along the way.

This thesis was prepared at The Charles Stark Draper Laboratory, Inc., under Draper Internal Research & Development Project 21181-001.

Publication of this thesis does not constitute approval by Draper or the sponsoring agency of the findings or conclusions contained herein. It is published for the exchange and stimulations of ideas.

As a member of the Air Force, I acknowledge that the views expressed in this thesis are mine and do not reflect the official policy or position of the United States Air Force, the Department of Defense, or the United States Government.

Benjamin L. Visser

[This page intentionally left blank.]

[This page intentionally left blank.]

Contents

List of Figures

List of Tables

[This page intentionally left blank.]

Chapter 1

Introduction

Society today is more dependant on space technology and national and international space assets than ever before, whether it be the Global Positioning System used in everything from wrist watches to guided munitions, global surveillance systems for watching the weather or ones enemies, and the multitudes of communications networks now using space technology for quicker, higher quality, global networks. Most of the satellites used for these purposes are large, and so are the vehicles used to launch them, which leads to very expensive and lengthy developmental and launch programs. There are only a few ways small satellites can be launched to space today, and most of them entail riding piggy-back with larger payloads on one of the existing launch vehicles. The cost to launch a small satellite, say less than one hundred kilograms, is still in the millions.

As an example Falcon-Sat 3, an United States Air Force Academy cadet developed, general-purpose satellite bus with various small experiments on board, was launched on 23 March 2007 as an additional payload aboard the new Atlas V Evolved Expendable Launch Vehicle (EELV). The Atlas V EELV "was designed to reduce launch costs by at least 25 percent over heritage Atlas, Delta and Titan space launch systems" [1]. This was the first time that an Atlas rocket was fitted with a secondary payload adaptor, allowing for six small spacecraft to accompany the primary payload into orbit. Falcon-Sat 3, with a mass of only 49.6 kg, was one of the secondary payloads, but its ticket for the ride to space still cost in the millions. In addition to that, the launch was delayed nearly seven months from the originally scheduled launch date due to program delays for the primary

payload, among other logistical reasons.

One of the mainstream technological trends of today is miniaturization. With continuing advancements in technology most electronic devices are getting smaller, thereby enabling space tasks and missions to be accomplished by smaller satellites. The need for cheaper space launch for smaller satellites is increasing. New companies, such as Space X and Kistler Aerospace, are stepping up this demand by developing space launch systems both on a smaller scale, and with more reusable components, thereby opening up the possibility for cheaper space launch. In addition, obtaining a launch system which demonstrates the capability of placing small payloads into orbit under an aggressive and responsive timetable delivers a dramatic tactical advantage to the nations or the corporations who have access to it.

An idea currently being investigated, and the topic of this paper, is a class of launch vehicles much smaller than the aforementioned ones. Imagine a rocket capable of bringing a payload on the order of two to six kilograms up to low earth orbit. Such a rocket is small enough to be carried by an aircraft, to an altitude where the atmosphere is thinner, potentially allow for a launch at a nose-high attitude to avoid a costly burn to turn the rocket, and add a modest about of velocity to the launcher before it even departs from the host aircraft. This would be similar to what Scaled Composites is demonstrating with its manned, suborbital White Knight rocket, which is carried high into the atmosphere by SpaceShipOne, before being released.

At the core of this problem is whether or not technology is currently far enough along to enable this mission, such as the sensors and other components of the launch vehicle being small enough in terms of both mass and volume, and also precise enough, and are there any missions that are able to be accomplished with the mass and volume limitations on the payload? A couple of possible mission profiles are presented in the next section which require low volume and mass for the payloads, while the rest of this thesis deals primarily with the sensor question. A form of statistical analysis, known as linear covariance analysis, is discussed and employed in a simulation to investigate how accurately a spacecraft of this size may be able to know its location in space relative to another vehicle that it wishes to rendezvous with, or at least closely encounter, and also

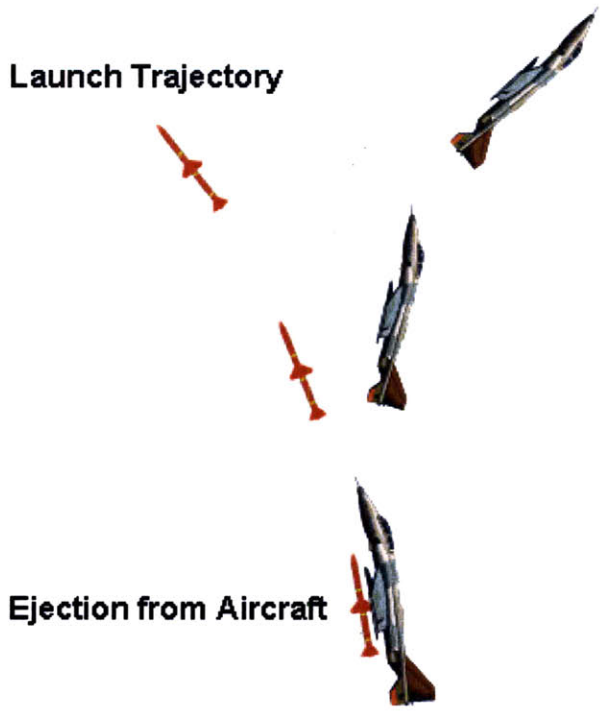

Figure 1-1: Potential Launch Vehicle Release Diagram

how accurately the spacecraft is able to follow a predefined, or nominal, trajectory to deliver its payload to a desired place at a desired time.

1.1 Problem Description

This thesis examines a new category of missions which will only be made possible by the continuing advancements in technology, specifically advances in miniaturization. Space launch and space manufacturing are approaching critical points, in which technology finally is close to enabling what was once only a part of the imagination. Tiny spacecraft, capable of performing anything from reconnaissance to refueling, will be able to be launched at a moment's notice, from anywhere on Earth.

The problem at the heart of this is whether or not currently available hardware, or that which is on the near horizon, will be both small enough and accurate enough to fit into the mass and tight volume constraints imposed for such a launch vehicle. This includes

everything from sensors like Inertial Measurement Units or star sensors, actuators in the form of reaction wheels, microthrusters, magnetorquers or otherwise, and the necessary electronic systems required to fully utilize all that is available to the spacecraft. This document primarily delivers a top level look at the Guidance, Navigation, and Control (GN&C) problem by employing simulation and Linear Covariance analysis to determine how accurately the spacecraft can know its position and velocity during a low earth orbit near-rendezvous type mission. The next section discusses some of the missions that this overall capability may encourage to be developed.

1.2 Mission Types

In the past it may have been tough to visualize what value a two to six kg satellite might have, but with the current trend of miniaturization of circuits, sensors, processors, instruments, and everything else electronic new possibilities are rapidly arising. Currently on the public market, one is hard pressed to find even an inertial measurement unit that that weighs less than this. The world, however, is currently on the verge of being able to provide complete avionics packages, sensors, and actuators small enough to enable missions that at one time were only fantasy. As these technologies continue to improve the percentage of the mass available for payloads, whether it is instrumentation, supplies, or anything else, will only increase. So what exactly could one do with such a small spacecraft?

Let us first consider a tactical ability that does not involve entering a closed orbit, but rather delivery of any type of supply, vehicle, or other equipment to any location on the globe, accurately, and at very short notice. Imagine an ICBM, but rather shrink it down to 1/100th scale, and replace the offensive payload with anything that might be critical to national security, whether it be a remote sensing autonomous ground or air based vehicle or equipment that may be critical to a forward deployed special operations team, the possibilities are endless. One primary concern of this type of mission would be landing accuracy, but as sensing instrumentation get better and smaller, this concern will be mitigated.

While on the topic of delivery type missions, it is not infeasible in the future to have a small spacecraft delivering fuel or new instruments to a much larger satellite which is already in orbit. Depending on the type of satellite, especially its mission, the orbit it is in, and fuel requirements, a modest amount of fuel can increase the lifespan of an existing satellite by a long time. One may envision a new sector of space industry in which a company creates a common access interface for refueling means, and then sells refueling missions to high-end customers, which may be mutually beneficial as the customer may save the millions or even billions it would cost to replace an aging fleet of spacecraft and the fuel company turns a profit on its individual missions.

A third example, and one that is more technically feasible today rather than tomorrow, would be a type of remote sensing mission in which the small payload would achieve near-rendezvous conditions with a spacecraft in orbit. By entering into a relative orbit, such as a natural-motion-circumnavigation (NMC) orbit, an orbit perturbed just a little in a precise way from the target spacecraft's orbit which allows the small satellite to passively move around and be able to take pictures of the target spacecraft for any number of beneficial reasons. The spacecraft may then transmit the pictures back to controllers on the ground, or to a space-based communications network already in place. This would allow for companies with expensive space assets to inspect their satellites for damage which may have occurred since launch, for military reconnaissance missions, and many other conceivable missions. If one is able to achieve near-rendezvous with a target spacecraft, then any other type of eavesdropping missions are also possible.

There are countless uses of space which have not been fully utilized due in a large part to the cost of designing and launching spacecraft, in a market where currently there are not many options for launching small payloads into orbit. Every year, however, more things become possible due to advancements in technology, and the need to launch small spacecraft will continue to increase. The nations and companies that embrace these changes and work to find people to develop the full potential of their space programs, both military and civilian, will benefit greatly.

1.3 Thesis Overview

Chapter 2 begins by introducing the method of Linear Covariance analysis. Included in this are motivations for the use of the method, compared with other methods available, such as Monte-Carlo analysis or high fidelity simulations. Also the mathematics behind Linear Covariance analysis are explained. The chapter continues on to explain some of the intricacies of the software used in the analysis of the mission, LinCov Tools. This includes how to create a nominal trajectory, how to setup the initial conditions for both the chaser and the target spacecraft, a discussion of the reference frames utilized, an explanation of the types of errors and sensors that the software has modeled, and finally how to interpret the covariance and dispersion results that the software produces. The chapter concludes with a detailed example.

Chapter 3 is all about the mission design. It begins by explaining in detail the three phases of the mission, from the time the rocket launches off of an aircraft to near-rendezvous in an 800 km orbit. It includes some background in astrodynamics and the rendezvous maneuvers used to accomplish the mission, and explains how the initial conditions were determined for the mission. In addition, the system hardware is examined, including the different systems and requirements, the unique enabling technology for this mission, and the different possible missile platforms and the tradeoffs between them.

Chapter 4 may best be described as the results chapter. Phase 1 of the mission, or the atmospheric part of the flight, is looked as by using a 3dof simulation to estimate the final position and velocity covariance at main-engine-cutoff. This data is then used as the initial uncertainty for the second phase of the mission, which is when the higher-fidelity LinCov Tools starts being utilized to look at the rest of the mission. In particular, phase two is approached using dispersion analysis to determine how accurately the spacecraft is able to follow its predefined nominal trajectory up to the target spacecraft's altitude, to arrive at a relative position behind the target. Phase three deals primarily with the relative covariance between the chaser and the target spacecraft during the near-rendezvous phase of the mission. This section details the need for some sort of relative position sensing, in order to enable the mission.

Chapter 5 summarizes the results found in the simulations, and conclusions are drawn as to the overall feasibility of this mission concept. The potential for future research is examined and suggestions are made as to the initial directions of focus to further this study.

[This page intentionally left blank.]

Chapter 2

Linear Covariance Analysis Primer

2.1 Introduction to Linear Covariance Analysis

Before going into some of the advantages, disadvantages, and details of Linear Covariance Analysis, the more classic type of statistical analysis used for Guidance, Navigation, and Control, Monte Carlo analysis, will be discussed. In Monte Carlo analysis, an n-dof simulation is developed to represent the dynamics of a certain system. For space missions this typically takes into account the spacecraft dynamics, atmospheric dynamics such as drag, control system dynamics, and more depending on the level of accuracy and fidelity required. Then hundreds or even thousands of simulations are run where certain parameters of interest are varied, such as the pointing accuracy of the spacecraft. After the data is all generated it is examined and studied to determine the system's sensitivity to the varied parameters. For a spacecraft this could be dispersions in position and velocity, delta-v, and navigation errors. An example of this type of analysis follows. Imagine a spacecraft which is initially resting in a 200 km parking orbit is then ordered to fire its thrusters to increase its orbital altitude to 800 km. Before the maneuver the spacecraft is moving with some velocity, V_o, and after the maneuver with velocity, V_1. A graphical representation of this lies below:

As can be seen, due to errors in the direction of the applied delta-v, the final velocity vector traces out a cone with interior angle equal to 2φ, where φ is the maximum attitude inaccuracy of the onboard navigation system, prior to the burn. The simulation uses

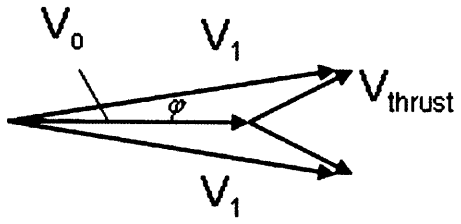

Figure 2-1: Thrust Attitude Dependency

simple 2-body problem dynamics, and works by integrating the non-linear equations of motion forward to find the point of closest encounter to 800 km in altitude for each case. The nominal, or zero degree of error, case is tuned so that the delta-v applied is the exact amount needed to perform a coelliptic transfer up to the target altitude, in half a period's time. What follows below is a plot of the position dispersion versus the onboard angular error:

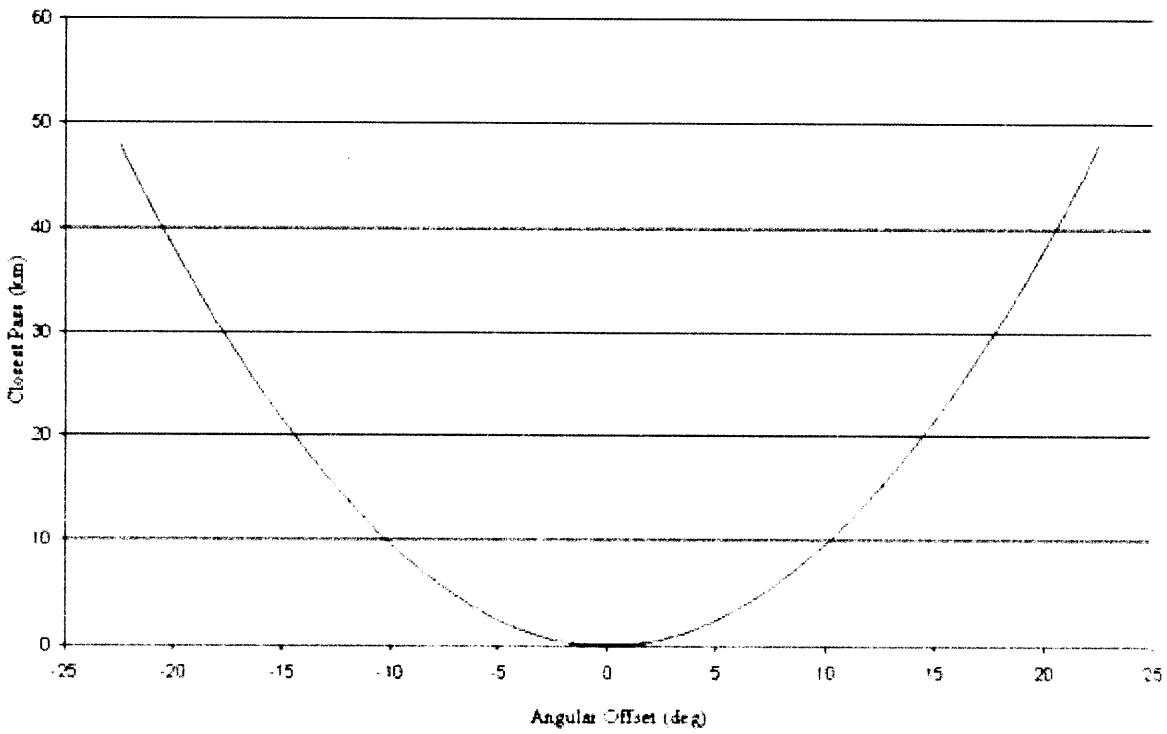

Figure 2-2: Position Sensitivity to Attitude Knowledge

The above example was fairly simplistic in nature, but if the effects of more variables on different aspects of the guidance, control, and navigation algorithms are required, the

number of runs required for Monte Carlo analysis begins to get very high. This is where Linear Covariance analysis comes into play. Essentially Linear Covariance analysis takes the complicated non-linear dynamics used when programming a simulation for Monte Carlo analysis and linearizes them over a nominal reference trajectory. Then a state covariance matrix associated with the chosen n-dof state vector is carried forward during the run and updated at each propagation step. These results are then approximations for the same fuel usage, dispersions from the nominal trajectory, and navigation errors found using Monte Carlo analysis, but they are obtained in only one run [2]. This shows one of the key advantages of Linear Covariance analysis, its speed. Onboard operations that were at one time limited by the computational requirements of a full Monte Carlo analysis can be efficiently performed using predeveloped linearized dynamics models. As a disadvantage, Linear Covariance analysis may take more time to develop initially since the dynamics have to be linearized, assumptions have to be made, and random processes must be represented as accurately as possible, usually by employing noise processes or Gaussian distributions, such as Equation 2.1, which depends on the standard deviation σ and the mean value μ.

$$f(x) = \frac{1}{\sigma\sqrt{2\pi}} e^{-\frac{(x-\mu)^2}{2\sigma^2}} \tag{2.1}$$

The approximations and assumptions that had to be made while developing the simulation do jeopardize some of the accuracy of the results, however for orbital dynamics this method has been proven to be quite accurate and the results to be a very good estimate of the actual full model results [2]. The next section will now explain the mathematics behind Linear Covariance analysis.

2.2 Mathematics of Linear Covariance Analysis

This section primarily summarizes the equations developed by David Geller in his paper "Linear Covariance Techniques for Orbital Rendezvous Analysis and Autonomous Onboard Mission Planning." For a more complete development of the navigation state and covariance algorithms please refer to Appendix A. Before starting it is important to lay

out the notation used in the following equations. A zero matrix is written as $0_{m\times n}$, an identity matrix will be referred to by $I_{n\times n}$, and a diagonal matrix will simply be written as $Diag(f)$ where the diagonal entries are f_1, f_2, etc. If ϑ is the angle of rotation about the unit vector $\mathbf{e}$, the quaternion which represents this rotation will be of the following format:

$$\mathbf{q} = \begin{pmatrix} \mathbf{e}\, sin(\vartheta/2) \\ cos(\vartheta/2) \end{pmatrix} \tag{2.2}$$

For normal vector rotations, the desired frame is represented as the subscript, while the current frame is shown as a superscript, so that T_b^i represents the direction cosine matrix which would bring a vector from the inertial frame to the body frame. Lastly, the distinction between which version of a variable is being referred to, whether it is a true value, nominal value, flight computer value, or measured value, is given by Table 2.1.

Desired Value	Notation
True	x
Nominal	$\bar{x}$
Flight Computer	$\hat{x}$
Measured	$\tilde{x}$

Table 2.1: Variable Designations

This study primarily deals with how well the space vehicle is able to know its own position and velocity, both inertial and relative to another spacecraft, as it tries to follow a nominal trajectory and maneuver for near-rendezvous. Thus the flight algorithms, or the navigation filters, are mostly what is of interest. Those familiar with Kalman filters will recognize the closeness of the algorithms to standard filtering ones, as they look first at navigation state and state covariance propagation, then navigation state and state covariance update, then navigation state and state covariance correction, and finally pointing, maneuver targeting, and control [2]. Equations 2.3 through 2.6 below represent the algorithm for navigation state propagation, update, and correction, with Equation 2.4 representing the Kalman gain.

$$\dot{\hat{\mathbf{x}}} = \hat{\mathbf{f}}(\hat{\mathbf{x}}, \hat{\mathbf{u}}, \tilde{\mathbf{y}}, t) \tag{2.3}$$

$$\hat{K}(t_k) = \hat{P}(t_k)\hat{H}_{\hat{x}}^T(t_k)\left[\hat{H}_{\hat{x}}(t_k)\hat{P}(t_k)\hat{H}_{\hat{x}}^T(t_k) + \hat{R}_\nu(t_k)\right]^{-1} \tag{2.4}$$

$$\hat{\mathbf{x}}_k^+ = \hat{\mathbf{x}}_k^- + \hat{K}(t_k)[\hat{\mathbf{z}}_k - \hat{\mathbf{h}}(\hat{\mathbf{x}}_k, t_k)] \tag{2.5}$$

$$\hat{\mathbf{x}}_j^{+c} = \hat{\mathbf{x}}_j^{-c} + \hat{\mathbf{d}}(\hat{\mathbf{x}}^{-c}, \boldsymbol{\Delta}\hat{\mathbf{u}}, \boldsymbol{\Delta}\tilde{\mathbf{y}}, t_j) \tag{2.6}$$

In parallel to the navigation state development, the navigation covariance goes through a similar process of propagation, update, and correction, as shown below in Equations 2.7 through 2.10, with Equation 2.8 once again representing the Kalman gain, which is used for the update step.

$$\dot{\hat{P}} = \left[\hat{F}_{\hat{x}} + \hat{F}_{\tilde{y}}\hat{C}_{\hat{x}}\right]\hat{P} + \hat{P}\left[\hat{F}_{\hat{x}} + \hat{F}_{\tilde{y}}\hat{C}_{\hat{x}}\right]^T + \hat{F}_{\tilde{y}}\hat{S}_\eta\hat{F}_{\tilde{y}}^T + \hat{S}_w \tag{2.7}$$

$$\hat{K}(t_k) = \hat{P}(t_k)\hat{H}_{\hat{x}}^T(t_k)\left[\hat{H}_{\hat{x}}(t_k)\hat{P}(t_k)\hat{H}_{\hat{x}}^T(t_k) + \hat{R}_\nu(t_k)\right]^{-1} \tag{2.8}$$

$$\hat{P}(t_k^+) = \left[I - \hat{K}(t_k)\hat{H}_{\hat{x}}(t_k)\right]\hat{P}(t_k^-)\left[I - \hat{K}(t_k)\hat{H}_{\hat{x}}(t_k)\right]^T + \hat{K}(t_k)\hat{R}_\nu(t_k)\hat{K}^T(t_k) \tag{2.9}$$

$$\begin{aligned}\hat{P}(t_j^{+c}) = &\left[I + \hat{D}_{\hat{x}}(t_j) + \hat{D}_{\Delta\tilde{y}}(t_j)\Delta\hat{C}_{\hat{x}}(t_j)\right]\hat{P}^{-c}(t_j)\left[I + \hat{D}_{\hat{x}}(t_j) + \hat{D}_{\Delta\tilde{y}}(t_j)\Delta\hat{C}_{\hat{x}}(t_j)\right]^T \\ &+\hat{D}_{\Delta\tilde{y}}(t_j)\hat{S}_{\Delta\eta}\hat{D}_{\Delta\tilde{y}}(t_j)^T + \hat{S}_{\Delta w}(t_j)\end{aligned} \tag{2.10}$$

The set of n true states are then augmented by the n navigated states to form the full system, as shown in Equation 2.11.

$$\mathbf{X} = \begin{bmatrix} \delta\mathbf{x} \\ \delta\hat{\mathbf{x}} \end{bmatrix} \tag{2.11}$$

With the augmented system in place, it is now possible to extract both the covariance

of the dispersion from the truth, or nominal, trajectory, and the covariance of the onboard navigation errors. The trajectory control performance is given by Equation 2.12 while the navigation performance is given by Equation 2.13.

$$D = E\left[\delta\mathbf{x}(t)\delta\mathbf{x}^T(t)\right] = \left(I_{n\times n} \;\; 0_{n\times\hat{n}}\right) P_x \begin{pmatrix} I_{n\times n} \\ 0_{\hat{n}\times n} \end{pmatrix} \tag{2.12}$$

$$P_{true} = E\left[\left\{\delta\hat{\mathbf{x}}(t) - C\delta\mathbf{x}(t)\right\}\left\{\delta\hat{\mathbf{x}}(t) - C\delta\mathbf{x}(t)\right\}^T\right] = \left(-C_{\hat{n}\times n} \;\; I_{\hat{n}\times\hat{n}}\right) P_x \begin{pmatrix} -C^T_{n\times\hat{n}} \\ I_{\hat{n}\times\hat{n}} \end{pmatrix} \tag{2.13}$$

Appendix A continues to further develop the specific models used for implementation of the algorithms presented above. Now that the equations of Linear Covariance analysis have been presented, the software used over the course of this study will be introduced.

2.3 Description of Lincov Tools

The software used to produce the covariance and dispersion results in this thesis is named Lincov tools. Essentially it is a direct implementation of the theory David Gellar developed, which was summarized in the previous section. Since it is a six state filter, it actively propagates, updates, and corrects the states, covariance, and dispersion matrices for a spacecraft's position and velocity. In order to propagate through maneuvers the software uses an estimated error in attitude, which is supplied by the user. Because of this one must look at the attitude sensors being utilized in the mission ahead of time to determine how accurately a spacecraft will know its attitude during the mission. For some of the results presented, this is introduced as a variable to the simulation so that exact knowledge of the sensors does not need to be known ahead of time; rather results are plotted versus the uncertainty in attitude.

For the majority of this study the benchmark inertial measurement unit (IMU) used is the Draper MMIMU, which has been commercialized into the Honeywell HG1930 MEMS IMU. It has a mass of less than 160 grams and volume of less than 66 cubic centimeters.

Figure 2-3 shows the commercialized version of the Draper MMIMU. The results for phase two of the mission are presented for IMUs of varying levels of accuracy, and also for varying levels of initial uncertainty gained through the atmospheric part of the mission.

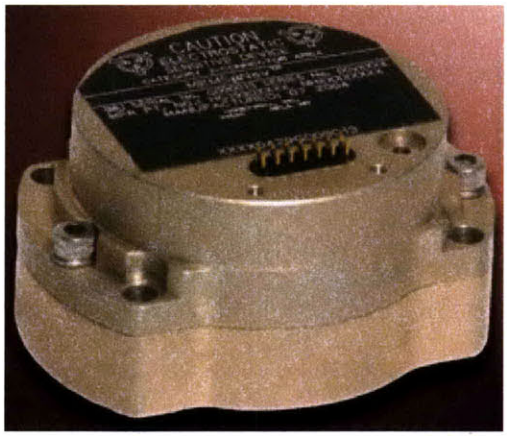

Figure 2-3: Honeywell HG1930 MEMs IMU

Physically Lincov Tools is programmed in the MATLAB environment. It has flexible controls for programming the nominal trajectory through function calls that are typical in space missions, such as coelliptics, v-bar and r-bar targeting, and Lambert routines. In addition it allows the user to establish a wide variety of sensor measurements and updates to be used during the mission, including GPS updates, ground position and velocity updates, relative optical camera measurements in the angles only or angles plus ranging mode, LIDAR measurements, differential GPS, and others. For Phase 2, the orbital transfer trajectory dispersion study, only an IMU with GPS capability is assumed once in orbit, with varying levels of angular knowledge and initial state vector covariance, depending on the results presented for Phase 1. For Phase 3 where the concern is the spacecraft's knowledge of its position and velocity with respect to a target spacecraft, simulations are done with and without the use of optical camera angles only measurements. Both cases assume the chaser has an IMU and is able to receive GPS updates to its position every one minute once it is in orbit.

2.3.1 Nominal Trajectory Generation

Lincov Tools was built with a few flexible routines for nominal trajectory generation. When combined appropriately, with well understood timing and spacing conditions, they may be used to develop a wide range of possible missions. For this study, primarily four different routines were used to establish the nominal trajectory from a low-earth-orbit parking orbit up to a natural motion circumnavigation (NMC) near-rendezvous orbit. These four are null burns, v-null burns, coelliptic transfer orbits, and Lambert targeting routines.

First of all, null burns simply attempt to maintain a spacecraft in its current orbit without allowing deviations from it. The user is allowed to define the length of time in hrs that this is maintained for. Secondly, v-null burns attempt to align the velocity vectors of the chaser and target spacecraft, in a curvilinear sense, and to zero out the difference in the magnitude of their velocities. For example, if the chaser spacecraft was approaching the r_{target} vector on an orbit with slightly lower semi-major axis, all other orbital elements kept constant, a v-null burn would increase the energy of the chaser spacecraft so that at the point exactly opposite on its orbit, it would now be slightly further out than the chaser vehicle, and their orbital periods would now be the same. This would be an open-loop method to enter into an NMC orbit about the target, however it is not generally used over Lambert targeting maneuvers. It is primarily used in this study to force the chaser spacecraft to "capture" the orbit of the target spacecraft, during an orbital transfer.

The next two type of maneuvers are variations of what is called the Orbital Boundary Value Problem. In this problem there are constraints that must be met, such as positions at certain times. In order to illustrate the geometry of this problem, Figure 2-4 has been included. The goal is to move a spacecraft at point P_1 with initial position $\mathbf{r_1}$ and initial velocity $\mathbf{v_1}$ to a point P_2 with final position $\mathbf{r_2}$ and final velocity $\mathbf{v_2}$. The transfer angle between them, θ, is measured from the central body located at focus F. In addition, sometimes the transfer time is used as a boundary condition, requiring that $\Delta t = t_2 - t_1$.

A coelliptic transfer is a type of maneuver which attempts to place the chaser spacecraft on an orbit that is slightly smaller or larger that the orbit of a certain target, and

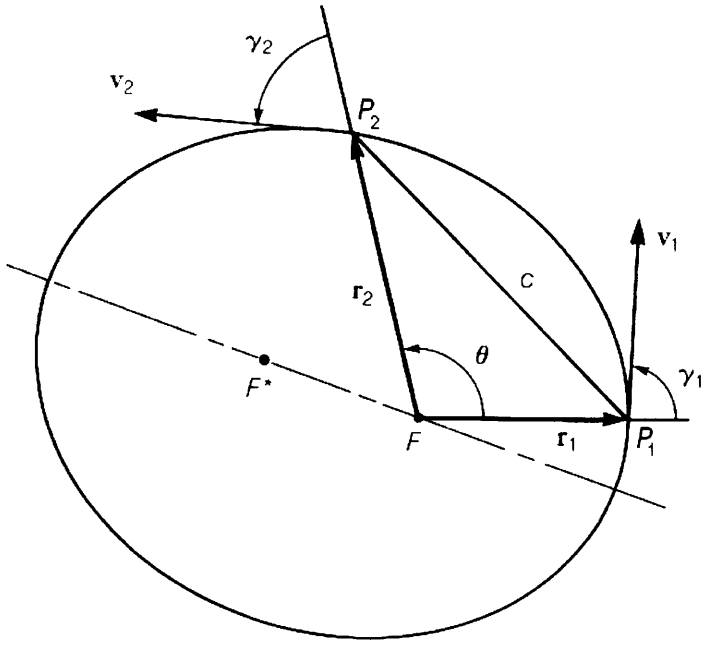

Figure 2-4: Orbital Boundary Value Problem [3]

while doing so tries to align the foci of the two orbits as much as possible. By doing this, the orbits stay roughly the same distance apart all the way around. For a circular orbit, where the ellipse's two foci collapse on the center point, a coelliptic transfer is simply a transfer that places a spacecraft into another circular orbit, slightly smaller or larger than the first one. Typically all of the other orbital elements, with respect to the angular orientation of the orbit about the central body, are kept the same, or are made to be the same. The transfer that takes place in 180 *deg* around the central body is the well-known Hohmann transfer. Space rendezvous is generally where the use of coelliptic transfers are seen today.

A Lambert transfer is a little more complicated than that a coelliptic transfer. Referring back to Figure 2-4, a Lambert transfer is when the two position vectors, r_1 and r_2, and the time of transfer, Δt, are known and the problem is to find the boundary velocities. Once the boundary velocities are determined the spacecraft software or the mission design team are able to determine burn magnitude and direction required to place the spacecraft on this transfer, and then to place it onto the final orbit. As the name implies, Johannes Lambert originally discovered the relationship between the geometric relationship of the

transfer orbit and the transfer time. Gauss then improved on Lambert's work and found a full solution, which was modified again in 1987 by Richard Battin of MIT, which removed a singularity in the solution method and improved convergence rates. It should be noted that there are always two solutions to the Lambert problem, and they travel opposite directions around the earth; usually only one of the two may be realistically applied. For more information on various types of solution methods to the Lambert problem, please refer to either Battin [3] or Vallado [5].

Lincov Tools has a nice setup for Lambert transfers in the nominal trajectory generation process, however it would need to be expanded if one wished to use it for non-rendezvous type operations, since the position it requires as an input is given relative to the target spacecraft. Equation 2.14 is an explanation of the reference frame it uses as its standard convention, where positive in the tangential direction is ahead of the target spacecraft, positive in the radial direction is further away from the central body, and the positive in the normal direction is chosen to complete a right handed coordinate system.

$$\mathbf{x}_{ref} = \begin{bmatrix} x_{tangential} \\ x_{normal} \\ x_{radial} \end{bmatrix} \tag{2.14}$$

2.3.2 Initial Conditions Setup

In order to accurately represent the position and future positions of an object in space, six independent quantities must be known. One of the most traditional ways to do this is to express the size, shape, and orientation of an orbit using the classical orbital elements, the last of which defines the current position of the space object on that orbit. Lincov Tools requires the initial conditions for the chaser and target spacecraft to be entered in as classical orbital elements, and then they converted to vectors in the Earth Centered Inertial (ECI) frame. The classical orbital elements are summarized in Table 2.2.

Semi-major axis describes the size of the orbit, and for elliptical orbits it is equal to half of the length of the major axis and for circular radius it is equal to the radius. Eccentricity describes the shape of the orbit. Circular orbits have an eccentricity of zero,

Classical Orbital Element	Designation
Semi-major axis	a
Eccentricity	e
Inclination	i
Longitude of the ascending node	Ω
Argument of pericenter	ω
True anomaly	ν

Table 2.2: Classical Orbital Elements

elliptical orbits between zero and one, parabolic orbits exactly one, and hyperbolic orbits greater than one. It is also equal to the ratio of the distance between the foci, $2c$, and the length of the major axis, $2a$, of an ellipse.

Inclination is the angle of tilt of the orbit, with orbits in the range of zero to 90 degrees being orbits that travel around the earth the same way it spins, and 90 to 180 degrees being retrograde orbits. Longitude of the ascending node is the angle between the primary axis (typically the $\hat{I}$ vector in the ECI coordinate frame) and the ascending node, or the location where a spacecraft would cross from the southern hemisphere into the northern. Argument of pericenter is the angle from the ascending node to the pericenter of the orbit, and true anomaly is the angle from pericenter to the current location of the object of interest. If the inclination is zero the longitude of the ascending node and the argument of pericenter are undefined, so alternate COEs represent them. Lincov Tools takes care of these conversions internally depending on the inputs. Figure 2-5 shows the details of the orientation of an orbit, with respect to the ECI coordinate frame.

The conversion between classical orbital elements and position and velocity vectors in the ECI frame is fairly straightforward. First of all, using only the size and shape of the orbit, and the current position of the spacecraft in that orbit, the position and velocity vectors are found in the perifocal coordinate system, PQW. This coordinate system is centered on the earth and is aligned with the orbit of the spacecraft. Then by using the orientation of the orbit with respect to the ECI coordinate frame, the $\mathbf{r}_{PQW}$ and $\mathbf{v}_{PQW}$ vectors may be rotated into the ECI frame. Complete discussion of this may be found in Vallado [5].

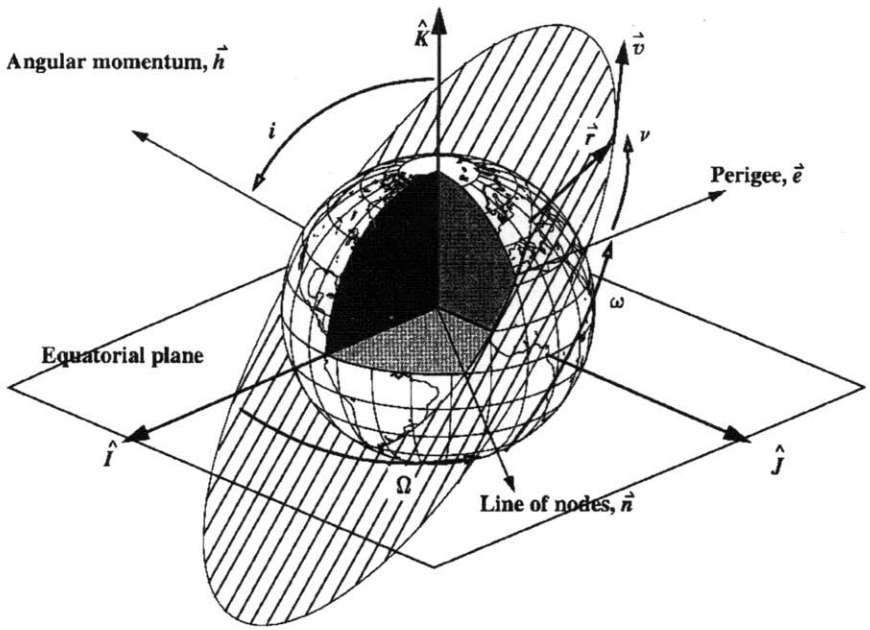

Figure 2-5: Classical Orbital Elements [5]

2.3.3 Reference Frame Discussion

The majority of the results presented in this paper will have errors listed in a body centric coordinate frame with downrange, cross-track, and radial components. The conversion between the Earth Centered Inertial (ECI) coordinate frame and this body frame is straightforward by using the algorithm described below. The radial direction is defined to be in the direction of the position vector of the spacecraft in the ECI coordinate system. The cross-track direction is defined as to be normal to the orbital plane of the spacecraft, in the direction which leaves the along-track (or downrange) vector, the 2nd vector in a standard right handed coordinate system, to be in the general direction of the spacecraft's velocity vector. Figure 2-6 shows this relationship.

Then if the vector $d\mathbf{r}$ is the position error vector in the ECI coordinate frame, the errors in the body frame can be found by using the algorithm found in Equations 2.15 to 2.19.

$$d\mathbf{r} = \mathbf{r}_2 - \mathbf{r}_1 \tag{2.15}$$

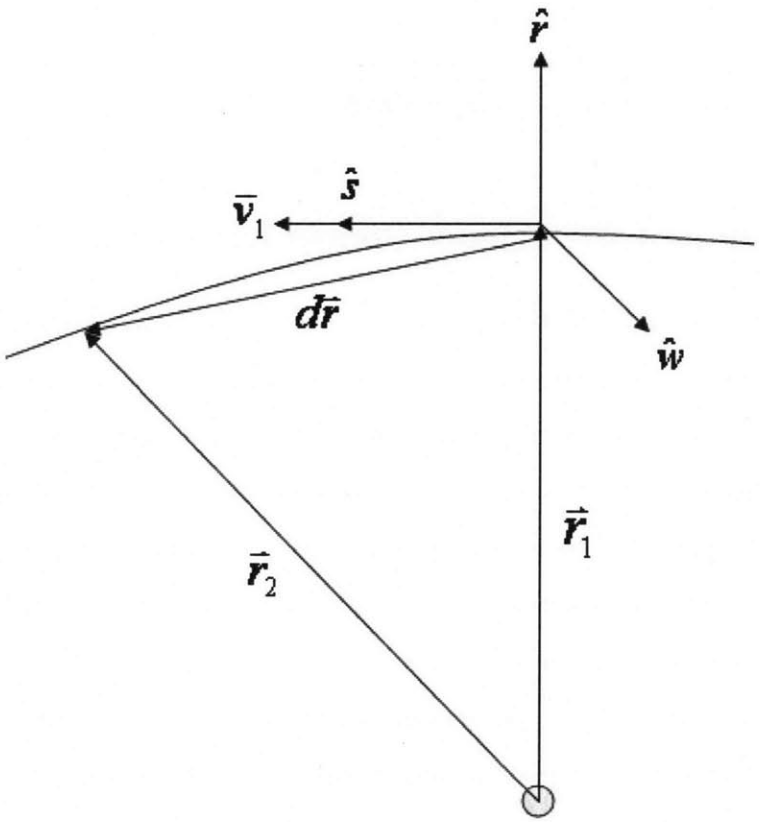

Figure 2-6: RSW Frame Vector Geometry

$$\hat{\mathbf{r}} = \frac{\mathbf{r}}{|\mathbf{r}|} \tag{2.16}$$

$$\hat{\mathbf{w}} = \frac{\mathbf{r}_1 \times \mathbf{v}_1}{|\mathbf{r}_1 \times \mathbf{v}_1|} \tag{2.17}$$

$$\hat{\mathbf{s}} = \frac{\mathbf{w} \times \mathbf{r}_1}{|\mathbf{w} \times \mathbf{r}_1|} \tag{2.18}$$

$$d\mathbf{r}_{\hat{\mathbf{r}}} = d\mathbf{r} \cdot \hat{\mathbf{r}} \qquad d\mathbf{r}_{\hat{\mathbf{s}}} = d\mathbf{r} \cdot \hat{\mathbf{s}} \qquad d\mathbf{r}_{\hat{\mathbf{w}}} = d\mathbf{r} \cdot \hat{\mathbf{w}} \tag{2.19}$$

2.3.4 Discussion of Covariance versus Dispersion

The primary results presented in this thesis will either be relative navigation covariance or navigation dispersion. The relative navigation covariance results will represent how well the chaser spacecraft knows its position and velocity in space relative to the target spacecraft at any time in the mission. For real missions a spacecraft also keeps track of its attitude and attitude rates, however this simulation does not propagate these values forward in time and instead uses metrics of gyro quality and other sensor information to determine an approximation of the spacecraft's attitude. The second type of data to be presented is navigation dispersion. Dispersion is a measure of how well the spacecraft is able to follow its predefined nominal reference trajectory. Both of these types of errors are highly dependent on many different sources of error, which are introduced in the next section of this thesis. For the most part, results will be in terms of relative covariance and dispersion. The fact that the covariance plots in this thesis represent a spacecraft's knowledge of its current state vector relative to another spacecraft's state vector makes general understanding of the quantity being examined a little more complicated. As an example, assume the spacecraft has an onboard GPS sensor, so that every so often, depending on the update rate, the spacecraft will know its own position and velocity within certain errors bounds, depending on the quality of the sensor and the atmospheric conditions which may affect GPS signals. For the sake of this study, modest values

for GPS accuracy are used: 50 m for position and 0.05 m/s for velocity. Therefore at each update one would expect the covariance of the spacecraft's position to jump within these bounds and drift upward until the next measurement, and then repeat the same behavior. However relative covariance not only takes into account the position and velocity of the spacecraft of interest, but also the target spacecraft, which the chaser spacecraft is trying to meet up with for a rendezvous or rendezvous-like mission. This will be better understood after reading about the sources of error.

This study will primarily look at dispersion for Stage 2 of the mission, where the goal is simply to follow a nominal trajectory and place a payload at a certain place in space at a certain time, which will then allow the spacecraft to be close enough to the target spacecraft to begin rendezvous operations, and will primarily look at relative covariance for Stage 3, which is the near-rendezvous part of the mission. The mathematics behind guidance, navigation, and control filtering result in the covariance of a spacecraft being driven down by additional absolute position and velocity measurements (such as ground updates, GPS measurements, etc) and by relative position and range rate measurements (such as optical camera, LIDAR, cooperative differential GPS measurements, etc). Relative measurements directly affect the relative covariance of the mission since they provide information directly related to the chaser and the target spacecraft's position and/or velocity. On the other hand, when concerned with the navigation dispersion a spacecraft builds during its mission, it is maneuvers that help drive the dispersion down. Small orbital corrections, midcourse burns, and other maneuvers help a spacecraft to determine exactly how close it is to its reference, or nominal, conditions.

Two types of plots will primarily be shown for the rest of the report. The first type is shown in Figure 2-7. This type of plot displays both the spacecraft's relative navigation covariance to its target spacecraft, and also its navigation trajectory dispersion. In this case the position information is shown; however a similar plot with the results for the velocity components may also be generated. The way to interpret these plots is fairly straightforward. The top one is showing how well the chaser vehicle knows its position with respect to its target, as a function of mission time. Therefore this result does not only depend on the vehicle's knowledge of its own position, but also the uncertainty involved

with the position of its target. For all simulations in this project it is assumed that the target spacecraft is uncooperative, meaning that it will not communicate its position to the chaser, nor broadcast updates on its position. It is also assumed that no updates on the target's position will be provided to the chaser from the ground. Therefore the uncertainty of the target spacecraft's position will always grow in time unless some sort of relative measurement can be made. This is in fact what is driving the error seen on the top plot. On the other hand, the bottom plot shows how well the chaser spacecraft is able to follow its nominal trajectory, dependant on its internal sensors. The dips just past the three hour mark are representative of those seen when the spacecraft makes maneuvers. For example, this occurs when the spacecraft has reached its target altitude and begins maneuvering to close in on the target spacecraft. The dispersion then grows again once it enters its NMC orbit about the target spacecraft and has smaller corrections to make.

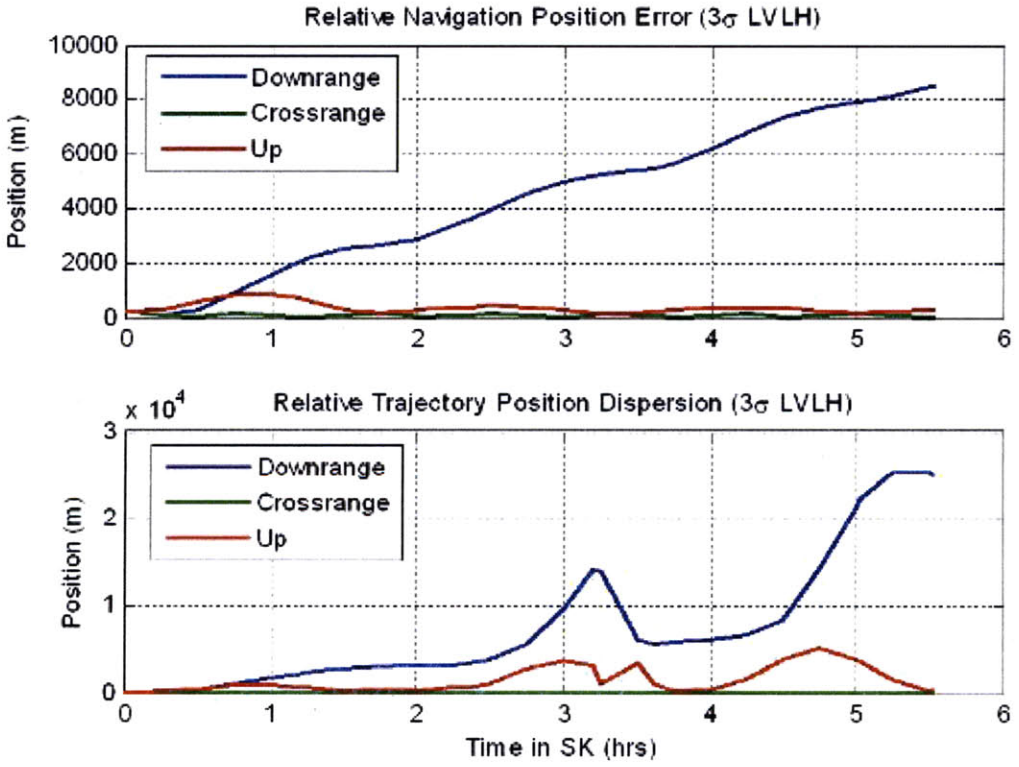

Figure 2-7: Example Covariance and Dispersion Plots

The second type of plot that will be presented chooses a single time in a particular mission, and then plots the vehicle's dispersion as a function of how well it is able to

know its attitude. Thus the requirement to define a single angular certainty before the simulation is removed and the effects of angular knowledge versus a spacecraft's ability to follow its nominal trajectory is developed. For Stage 2 of the mission, the point of interest lies at the end of spacecraft's journey up to its target altitude. The dispersion at this end point defines an error basket, or error ellipsoid, of possible chaser spacecraft positions about the desired place in space. Figure 2-8 shows an example of this type of plot.

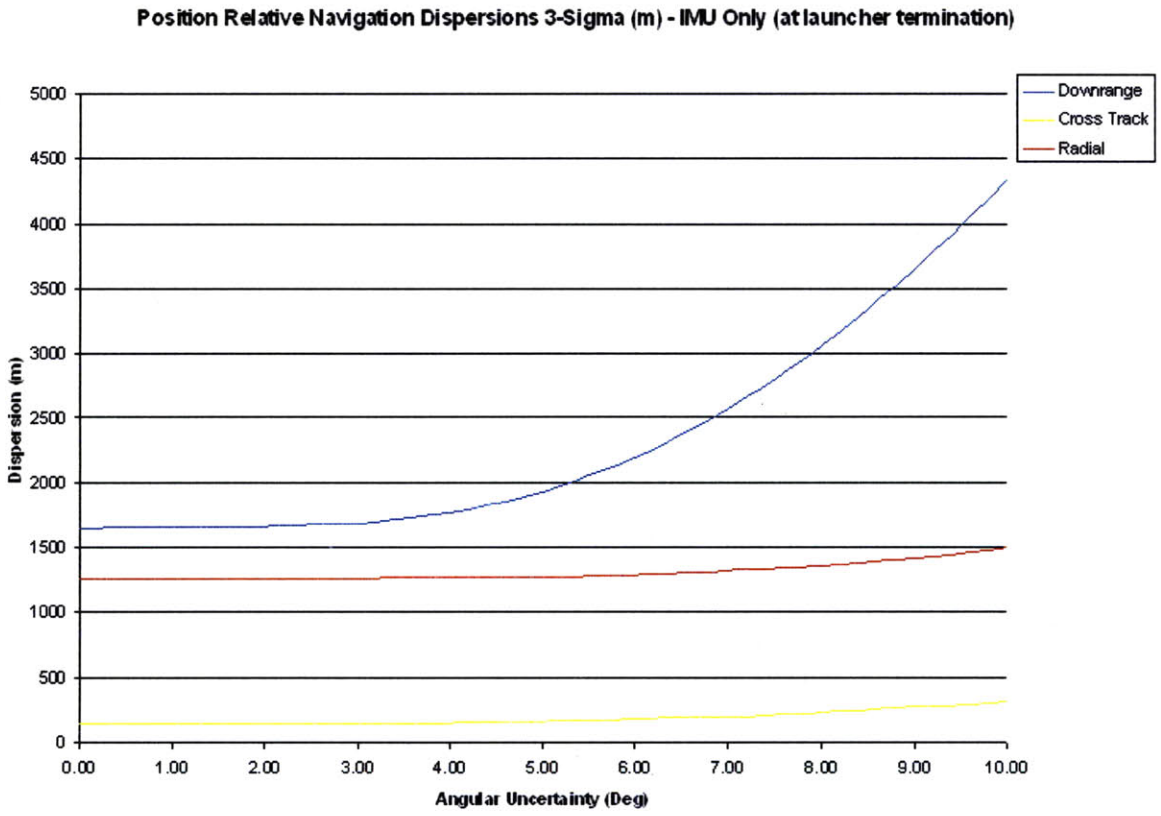

Figure 2-8: Example Dispersion versus Angular Uncertainty Plot

2.3.5 Discussion of Error Types

The total errors found in the two types of plots explained in the last section are combinations of many different sources which Lincov Tools accounts for. Table 2.3 lists the six broad categories of errors that the software models. Each type of error then has variables

which the user may modify in order to define the accuracy of the sensors and information being supplied to the spacecraft.

Error Type	Acronym
Chaser Position Update Error	CPUE
Unmodeled Acceleration Noise Density	UAND
Passive Vehicle Initial Covariance	PVIC
Active Vehicle Initial Covariance	AVIC
Maneuver Knowledge Error	MKER
Maneuver Execution Error	MEER

Table 2.3: Modeled Error Types within Lincov Tools

First of all there is chaser position update error (CPUE). This effect is seen when GPS or ground updates are enabled in the software so that the chaser vehicle is continually receiving new knowledge regarding its position in space. For all the simulations accomplished here it is defaulted to 50 m, a modest estimate of what one can obtain in low-earth-orbit using GPS. The second type of error is unmodeled acceleration noise density (UAND). This error attempts to account for unmodeled perturbations to the vehicle's movement, such as from the effects of higher order geodetic models, atmospheric drag, etc. It is set to be 4e-13 m^2/s^3. A third type of error is passive vehicle initial covariance (PVIC). This accounts for errors in the knowledge of the target spacecraft's position at the start of the mission. Since no updates are received for the target spacecraft's position after launch this initial number is what is seen getting worse over time until relative measurements may be made. For the sake of this study it is always initialized to be 50 m. The fourth type of error is active vehicle initial covariance (AVIC), which is the error in the position and velocity of the chaser spacecraft at the start of the mission. The values used here differ significantly, and depend on the quality of the onboard inertial measurement unit (IMU). The results from the atmospheric launch part of the mission are used to supply the information to this variable, and analysis later will show how important it is for a spacecraft to know its own position and velocity accurately before making large maneuvers. A fifth type of error is maneuver knowledge error (MKER). This error accounts for how well a spacecraft is able to sense its own maneuver's magnitude and direction, as it is occurring, in order to internally propagate its position and attitude knowledge

forward in time. Essentially these errors are used to tune how accurate the spacecraft's navigation system is during maneuvers. The final type of error looked at is maneuver execution error (MEER). This error accounts for how accurately the spacecraft is able to perform a maneuver, once it is given the instruction to do so, in terms of both magnitude of maneuver and direction of maneuver. The effects of thruster misalignments, throttling and start/stop errors, and others are seen here. Figure 2-9 shows a breakdown of the errors for a sample run. It is important to note that these errors, like most statistical errors, add in a Root-Sum-Squared (RSS) sense, not linearly.

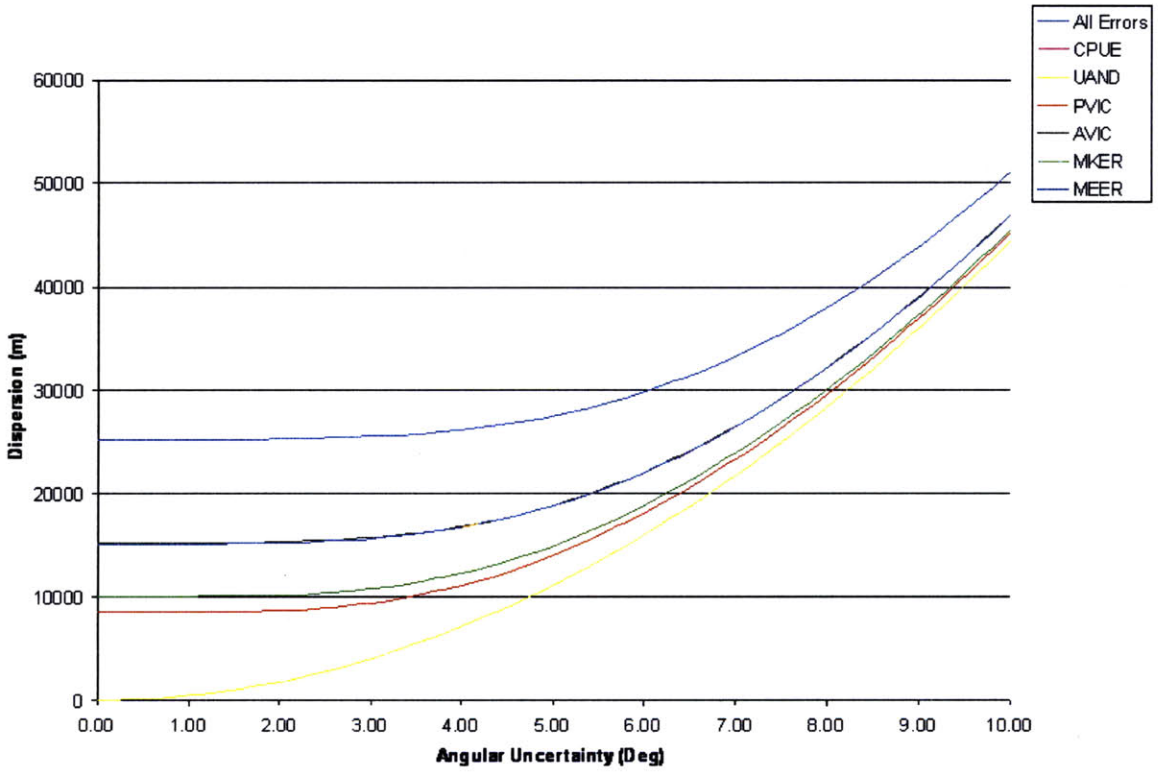

Figure 2-9: General Sources of Error Plot

2.3.6 Discussion of Measurement Types

This section will detail the different types of measurements and sensors that the version of Lincov Tools used for this analysis has modeled and the parameters which are user definable. As mentioned in the last section, GPS measurements are available for the chaser spacecraft. The time delay between measurements may be chosen to be any number of

seconds, defaulted to 60 *secs*. In addition, the accuracy of the measurements may be defined for the position updates, which then directly affect the calculated updates to velocity that the onboard navigation system is able to deduce. In general, 50 m is the default value used for this analysis. The software also allows for a cooperative target, meaning that the target is assumed to be able to obtain its own GPS updates, it may broadcast them to the chaser spacecraft which subsequently are used for GPS range and range-rate evaluations. It is assumed that the target spacecraft is not cooperative for this study.

The next sensor that the software has modeled is a LIDAR, used primarily for close-in operations, such as rendezvous. Both angular and ranging information are available by using this type of sensor, but it is possible to allow only one or the other modes to be activated if it is deemed appropriate. Each measurement type has a specified time delay between subsequent measurements. A LIDAR was not used for this research, due primarily to the size and mass of currently available instruments, which are too large for the small class of mission being evaluated. The LIDAR model is quite complex, and allows for user inputs for quantities such as maximum acquisition range, angle measurement noise, aggregated angle measurement bias and bias time constant), common-mode measurement noise, bias, and bias time constant, range measurement noise, bias, and bias time constant, and finally range rate measurement noise, bias, and bias time constant. In addition, different values are allowed for the truth model and the navigation filter model for all the above variables. Another sensor not used but available is a radio direction finder (RDF). This is used for differential phase measurements. The truth and filter noise constants, field-of-view, and update rates may all be defined for this type of sensor.

Primarily for all of the runs presented in this thesis, the only measurements being used come from the inertial measurement unit and depending on the phase of the mission, Global Positioning Satellites. However, for Stage 3, the near rendezvous portion, the effectiveness of a visual camera in providing relative covariance information to the chaser spacecraft is evaluated. This is the last type of measurement that Lincov Tools allows. Like all of the other measurements, the time delay between measurements may be defined. Also, for very close-in operations, a built-in function allows for image-size range

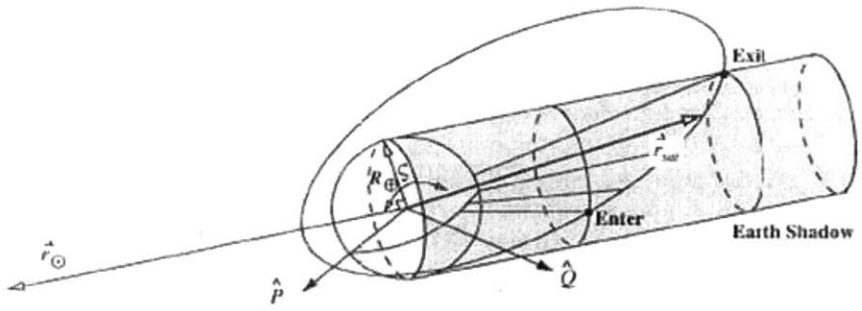

Figure 2-10: Geometry of the Cylindrical Eclipse Approximation [5]

measurements. This option is not utilized since the goal here is to never get closer than a five by ten km football orbit around the target spacecraft. Other parameters that may be varied are maximum range for acquisition, minimum range for use, maximum range for range measurements (not used), angle measurement noise, aggregated angle measurement bias and bias time constant, and common-mode measurement noise, bias, and bias time constant. Once again these values may be set independently for both the truth model and the navigation filter model. It should be noted that the simulation uses a simple cylindrical approximation for earth eclipse conditions in order to determine when visual camera measurements may be made, which for low-earth-orbit is fairly accurate. Figure 2-10 shows the geometry of the eclipse problem, and solution methods for determining when a spacecraft is in eclipse may be found in Vallado [5].

2.4 Complete Example

In order to better show how a mission is created and the type of results generated from Lincov Tools, a simplified example will be presented in this section. Two spacecraft are chosen to be on circular, equatorial orbits, $\mathbf{r}_c$ with an altitude of 200 km and $\mathbf{r}_t$ with an altitude of 400, with an initial angular spacing $\theta = 45deg$. Figure 2-11 shows the initial conditions geometrically.

For this example problem, everything is going to be kept real simple. The mission will simply be that the chaser spacecraft stays put on its initial orbit for 3.5 hrs. Based on the initial positions of the spacecraft, and knowledge that smaller orbits have smaller periods,

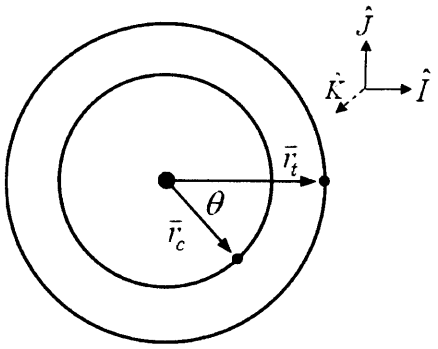

Figure 2-11: Example Problem Initial Conditions

it is expected that the chaser spacecraft will slowly catch up to the target spacecraft, and eventually pass it. It is important to look at the nominal trajectory that the software thinks you wanted before looking at the relative navigation covariance and dispersion plots, as occasionally it requires some tweaking. Trajectory plots for this simulation are included in Figure 2-12. It may be seen that the nominal trajectory being used in the simulation is indeed what was requested. The relative altitude remains at -200 km, the relative cross-track remains at 0 km, and the relative downrange slowly decreases during the 3.5 hr mission. The black dots on the plots indicate when the target spacecraft is in eclipse. As a side note, with orbital altitudes of 200 to 400 km, the spacecraft will travel around the earth roughly once every 1.5 hrs.

The last thing to do is to setup the instrumentation suite and measurement errors that are desired. The simulation is run with a step size of 60 sec and the only two sensors being utilized are GPS position updates every 1 min for the chaser spacecraft, and the Honeywell HG1930 IMU. The chaser position update error is set to 50 m. A visual camera would not be useful here as even during the closest encounter between the two spacecraft the chaser is too far away to pick up the target; the camera will be used during the full mission, however, to show the effectiveness it has in driving down the relative navigation covariance. Also, it will be assumed that the initial position and velocity of both spacecraft are known accurately up to 50 m and 0.05 m/s, respectively. The navigation position and velocity results may be seen in Figures 2-13 and 2-14.

As can be seen on the plot of navigation position error, or covariance, the downrange

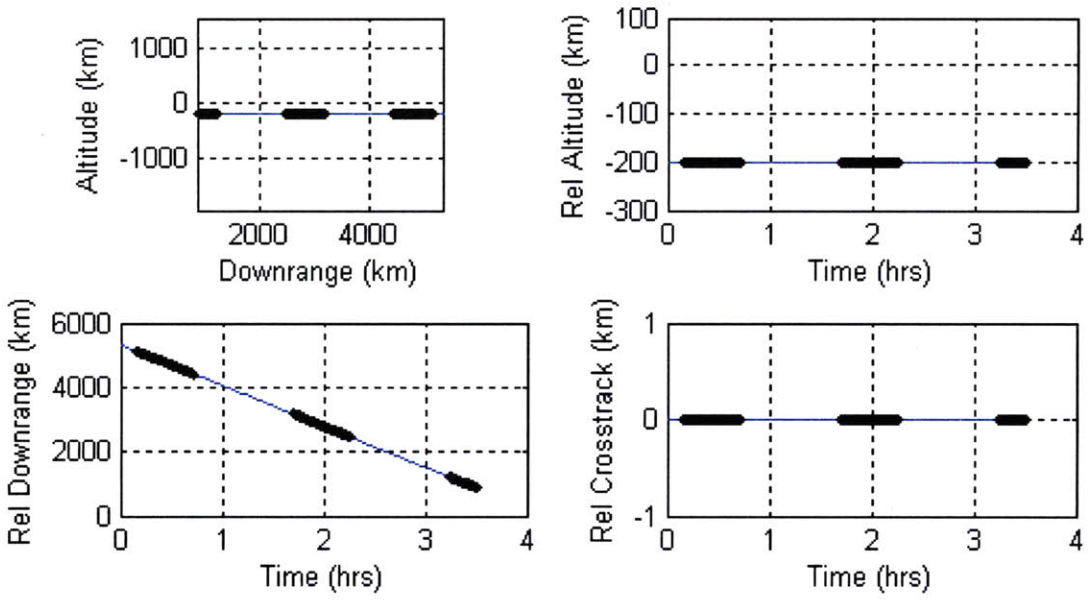

Figure 2-12: Example Problem Nominal Trajectory Plots

component of the error is the greatest. This will continue to be a trend throughout most of the analysis presented in this report, and makes good sense seeing as how the component of the velocity vector in the downrange direction is almost always far greater than the other two components. Therefore errors in the integrated velocity, or position, will be larger as well. Another aspect of these plots is that the results are typically somewhat periodic in nature, while also following a general direction.

All of the plots presented here, position and velocity, are divergent in their total error. Since this is such a simple mission being looked at, that is rather expected. No relative measurements are made between the chaser and the target spacecraft so the position and velocity navigation covariance results are never corrected due to new information. While it is true that the chaser is receiving GPS updates on its own position, it never receives updates on the position of the target spacecraft, and this is mostly what is driving the errors up over time. Regarding the position and velocity trajectory dispersion plots, no maneuvers are performed throughout the course of this mission, so the spacecraft never has a chance to correct its path through space to more closely follow the nominal trajectory, even though the spacecraft knows that it is departing from it over time. For

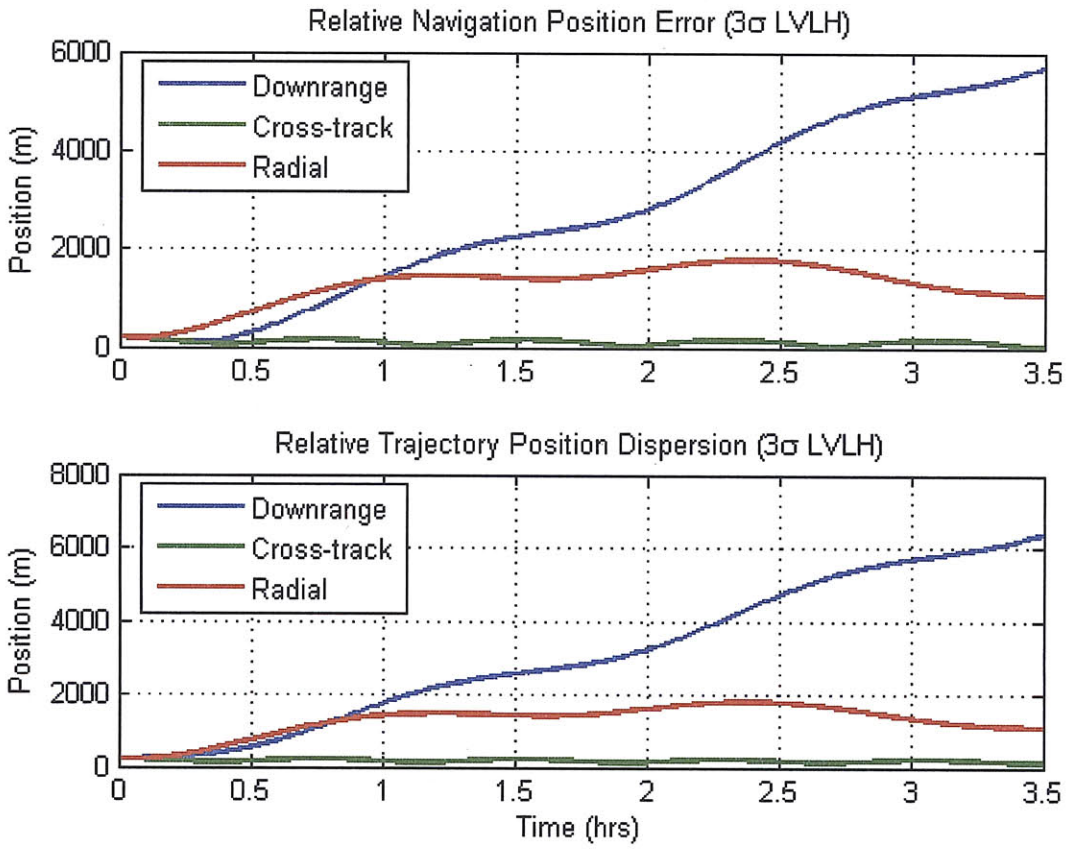

Figure 2-13: Example Problem Relative Navigation Position Covariance and Dispersion

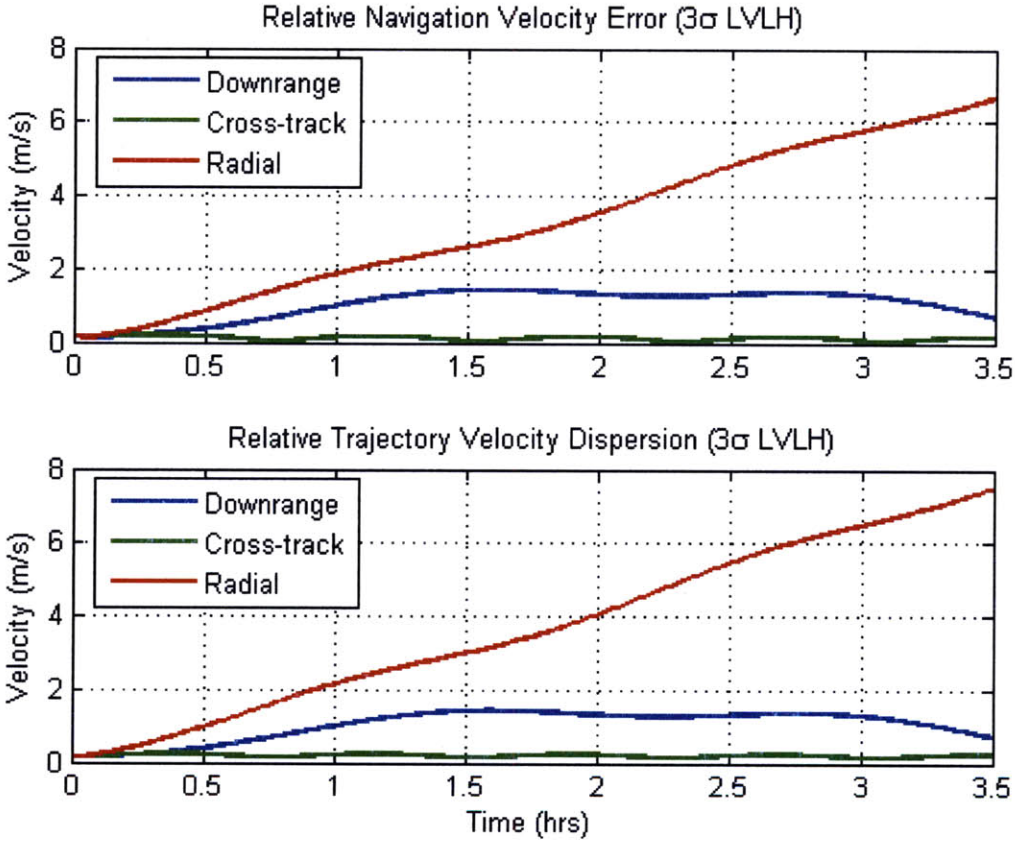

Figure 2-14: Example Problem Relative Navigation Velocity Covariance and Dispersion

the more complicated mission to come, much more dynamic plots will be encountered and will provide better insight into the navigation filter's performance.

Chapter 3

Mission Design

3.1 The Three Phases of the Mission

As previously mentioned, this study is concerned with a near rendezvous mission after being launched from a fighter type aircraft. The first phase of the mission is the atmospheric flight phase, up until the spacecraft reaches an orbital altitude of 200 km. The second phase is primarily the orbital raising phase of the mission, where the spacecraft desires to follow a nominal trajectory to place it close enough to the target spacecraft to begin rendezvous type maneuvers. And of course the last phase is when the chaser spacecraft maneuvers from approximately 50 km behind the target spacecraft into a closed relative orbit about it.

The class of satellites being examined is so small that it is intuitive to think that they may be involved in missions where one or more of them link up, or fly in a constellation, to perform a mission greater than just one can do by itself. When multiple spacecraft are concerned, and each one is launched individually from an aircraft, many considerations such as launch spacing, orbital phasing, and minimum fuel rendezvous schemas become important. This work primarily looks at the performance of a single launch vehicle with its payload. In turn, this knowledge may be used in the mission planning and orbital design for a multiple spacecraft mission. For example, say it is found that one of these spacecraft, dependant on the set of sensors, actuator hardware, and other constraints, is able to fly up to an orbit 800 km in altitude while maintaining within five kilometers of

its nominal trajectory. Then it is up to the risk management and design teams working together to decide how closely to phase multiple spacecraft. They are going to have to decide on a factor of safety so that the spacecraft stay far enough part from each other so that statistically a collision will not be possible. Once the spacecraft are close enough together that their sensors can detect each other and their software begin to reduce the error baskets around the vehicles, they may begin to move closer to each other and subsequently towards the target vehicle in space.

3.1.1 Atmospheric Launch

The first phase of the mission will be looked at mostly independent of the follow-on phases. The rationale for this is that the launch of the rocket from a fighter is a rather flexible event, and may occur any number of minutes, or even hours before it is desired for the spacecraft to begin to increase its orbit up to the target spacecraft's orbital altitude. The main thing with the atmospheric launch phase is that the rocket is able to place the spacecraft into a low-earth-orbit at an altitude of approximately 200 km, and that it does its best to minimize the uncertainties in the spacecraft's position, velocity, and attitude to allow the rest of the mission to be a success. It is undesirable for, say an F-15, to climb to an altitude over 50,000 ft because doing so requires special gear for the pilots, among other considerations. Since launching from a nose-high attitude is needed to avoid a costly turn in the rocket's direction at launch, this places limits on the altitude and speed that the rocket should be fired. In addition, most missiles are fired subsonically for military applications, and it is after separation that the missiles go supersonic; therefore this will become a constraint as well. In order to meet all of these constraints it has been decided that the launch altitude will be 36,000 ft and that the speed of the fighter will be close to Mach 0.8, approximately 265 m/s. It is assumed during the launch phase that GPS is not available until reaching low-earth-orbit, due to atmospheric distortion of the signal, a worst case type scenario. However the rocket is provided position and velocity information at launch by the aircraft. A 3 degree-of-freedom simulation was then used to find an estimate for the navigation position covariance at main-engine-cutoff, once the rocket places the spacecraft into a 200 km orbit, as a function of IMU performance. A

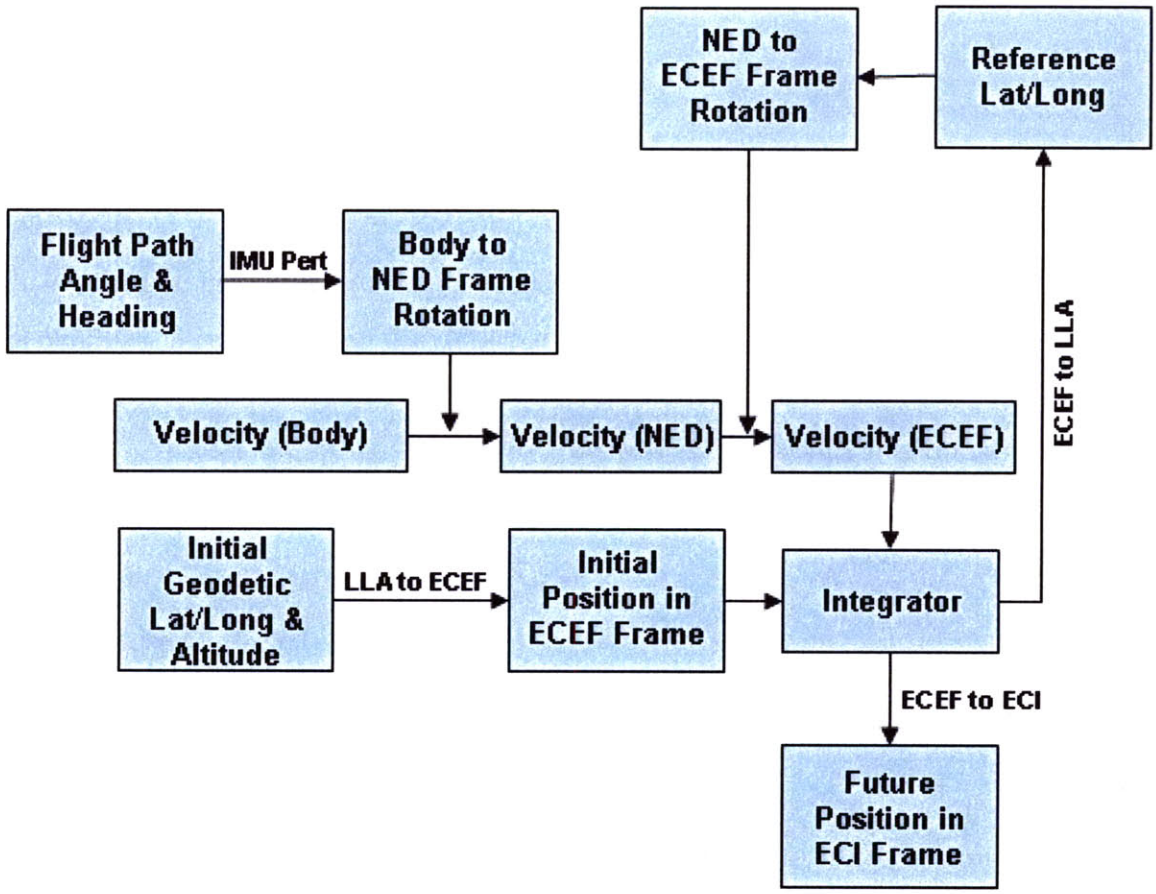

Figure 3-1: Phase 1 3-DOF Simulation Flow Chart

flow-chart for the basic function of the simulation is shown in Figure 3-1. It is important to know that LLA stands for the Latitude-Longitude-Altitude coordinate frame, NED refers to the North-East-Down body coordinate frame, ECEF is the Earth-Centered-Earth-Fixed coordinate frame, and finally ECI is the stand Earth-Centered-Inertial coordinate frame.

The way that the simulation works is fairly straightforward. Given a launch latitude, longitude, and altitude, and time history approximations for flight-path-angle, heading, and velocity of the rocket, the initial position and the velocity vectors are rotated into the ECEF frame, and then integrated forward in time to find the future values for the position of the rocket in the ECEF frame, which is then rotated back into the LLA frame to form a new NED2ECEF rotation matrix, and rotated into the ECI frame for analysis. The

Body2NED rotation matrix changes throughout the simulation depending on the time history data for the flight-path-angle and the heading. The simulation is then broken into two parts, one as described above to find the "truth" ECI position vectors, and one where the flight-path-angle and heading values are perturbed due to errors accumulated by the onboard inertial-measurement-unit, so that the Body2NED rotation matrix is also perturbed forming a new set of ECI position vectors for the non-perfect system. The results are then compared to find the position navigation covariance during the launch phase of the mission. This data is subsequently used within Lincov Tools to accomplish to the rest of the mission analysis.

3.1.2 Orbit Raising

As previously mentioned, the tie between the launch phases and the orbit raising phases of the mission is a timing constraint. The atmospheric phase only lasts for approximately 6.5 *mins* so depending on how quickly an aircraft can get to the launch position the amount of time spent waiting in orbit for proper transfer timing may be more or less. For this study, since the goal is to evaluate the performance of the navigation filters, a modest on orbit wait time will be assumed by the choice of initial conditions for the chaser and target spacecraft. Phase 2 and Phase 3 of the mission is programmed as a single nominal trajectory in Lincov Tools, however the data being looked at and the mission time that it is being looked at will vary based on what knowledge is desired. Phase 2 is concerned with how well the spacecraft can follow a predefined trajectory, independent of a target, in an effort to determine how accurately the payload may be placed at a certain place at a certain time. Once this is known the mission design team may decide what is an acceptable distance to attempt to place the chaser away from the target before relative operations are able to take over. Phase 2 primarily is coelliptic transfer problem, from 200 km to 800 km. The modest wait time at the 200 km will still be maintained, however, to more accurately represent what a standard space mission will be like, and also to solve a problem with initial position and velocity covariances which will be explained later. An initial spacing between the chaser and target spacecrafts of $\theta = 90\ deg$ will be used, just as in the example problem, except that this time the target vehicle begins at 800 km

	X	Y	Z
Position (km)	4651.445	-4651.445	0.000
Velocity (km/s)	5.5043	5.5043	0.0000

Table 3.1: Chaser Spacecraft Initial Conditions

	X	Y	Z
Position (km)	7178.137	0.000	0.000
Velocity (km/s)	0.0000	7.4518	0.0000

Table 3.2: Target Spacecraft Initial Conditions

instead of 400 km. Figure 3-2 is included again as a reminder to the mission geometry. Therefore the initial conditions in the ECI frame for both vehicles may be seen in Tables 3.1 and 3.2.

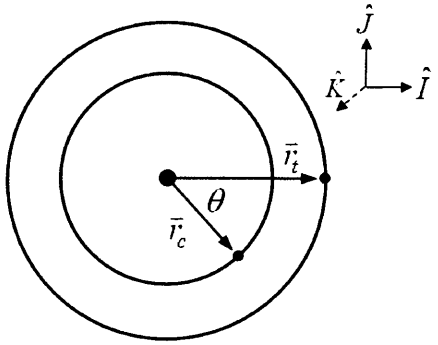

Figure 3-2: Full Mission Initial Conditions

Finally, Figure 3-3 shows a side view of the mission, where the black dots represent the eclipse condition and the red dots represent maneuvers. As can be see on these plots, the altitude is indeed raised up to the target spacecraft's altitude, the relative cross-track remains zero, and the spacecraft catches up so that it is now only 50 km short of the target spacecraft. The last red dot on these plots indicate a v-null burn used for stationkeeping at the desired point. It is from this point that the Phase 3 rendezvous operations begin.

3.1.3 Near Rendezvous Operations

The last section stated that the chaser spacecraft arrives in target spacecraft's orbit 50 km behind it. This did not just happen by chance, it takes careful planning to determine

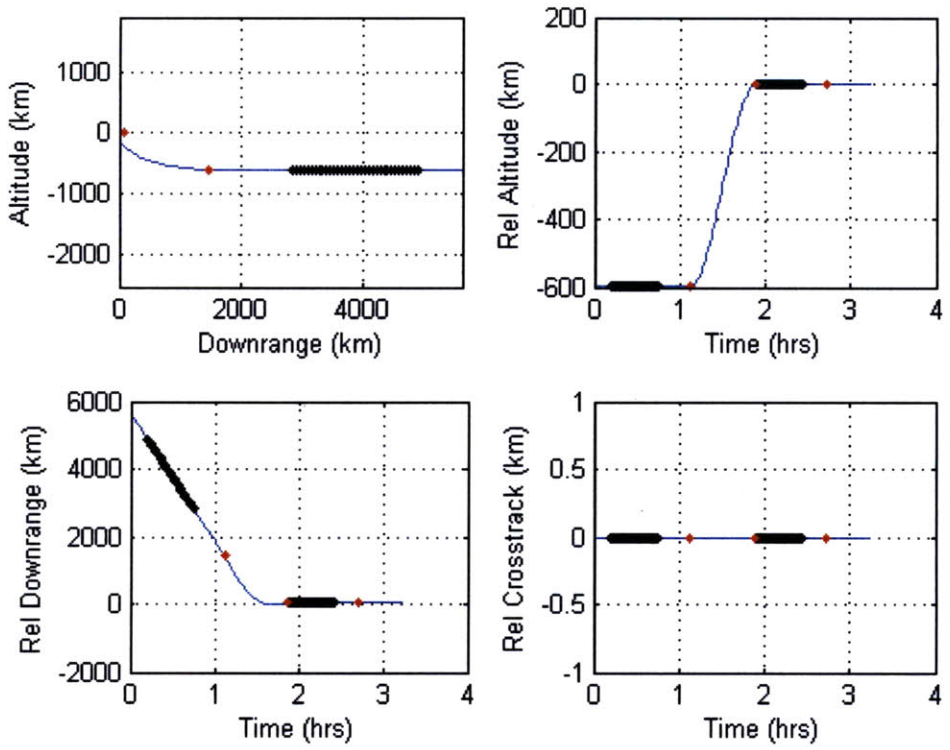

Figure 3-3: Mission Profile: Phase 2 Relative Position Plots

how much time to wait in the parking orbit at 200 km before firing the second-stage engines to transfer up to 800 km. The semi-major axis of the transfer orbit is equal to the arithmetic average of the semi-major axes of the orbits it connects which in this case is simply the radii, as seen in Equation 3.1.

$$a_{ph} = \frac{|\mathbf{r}_t| + |\mathbf{r}_c|}{2} \tag{3.1}$$

By applying the relationship between semi-major axis and orbital period in Equation 3.2, divided by two since the transfer is half of a period, it is found that the transfer from 200 km to 800 km takes 2838.5 sec.

$$TOF_{ph} = \pi \sqrt{\frac{a_{ph}^3}{\mu}} \tag{3.2}$$

If the transfer is done immediately at the start of the mission, the chaser spacecraft will have traveled 180 deg around the earth and the target spacecraft 168.84 deg, so that now

the target is 33.84 *deg* ahead on its orbit. Apply the relationship found in Equation 3.3 to find that being 50 *km* behind in an 800 *km* orbit is equivalent to a lead angle of 0.399 *deg*.

$$\phi_{des} r_t = lead_{dist} \tag{3.3}$$

Therefore the chaser spacecraft must catch up by a central angle of 33.44 *deg*, or 0.584 *rad*, if it is to arrive precisely 50 *km* behind the target. Apply the last condition found in Equation 3.4 to find that the chaser must wait 4028 *sec*, or 1.13 *hrs*, before firing its second stage and entering the transfer orbit.

$$t_{start} = \frac{\phi_{behind}}{\omega_c - \omega_t} \tag{3.4}$$

Now that the nominal trajectory is setup to place the chaser spacecraft 50 *km* behind the target spacecraft, it is time to be concerned with how exactly to proceed with entering into a near rendezvous orbit. First of all, a v-null burn will be performed at this point leaving the chaser here for half of a period, to try to allow it to get a better sense of the target if it has relative sensing capability, which will be shown later to be essential for mission success. Throughout the history of rendezvous operations, many different approaches have been used. Typically a spacecraft is directed to a couple stable-orbit rendezvous points, which the point in this mission at 50 *km* may be referred to as. Then slowly the spacecraft works its way in to the target over many periods. An example of this may be seen in Figure 3-4, which is a diagram of how the shuttle works its way in to different targets, mostly the International Space Station today. Once it gets very close the rendezvous operations become much more complicated, but for this mission the closest approach is 5 *km* so it is a little less complicated.

The nominal trajectory for this mission will proceed by slightly lowering the orbit of the chaser after the half-period wait at SOR point number 1, and over the course of a quarter period will target using a Lambert burn a point exactly 10 *km* behind the target spacecraft, which will be called SOR point number 2. It will then stop there for another half of a period of station keeping and target acquisition. After this the hard part of the mission begins, which is when the chaser spacecraft attempts to enter into a 5 by

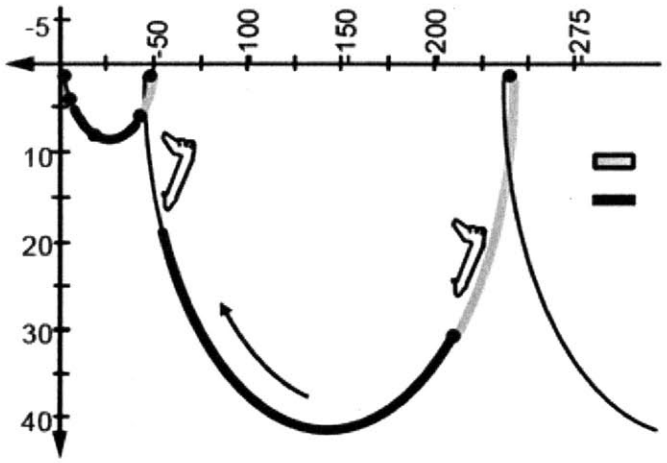

Figure 3-4: Space Shuttle Stable Orbit Rendezvous Trajectory [7]

10 km football orbit around the target vehicle. A Lambert transfer is used to target a position exactly 5 km below, or towards the earth, of the target vehicle, with a transfer time of a quarter of a period, and then when it arrives there another Lambert transfer is immediately used to target a point exactly 10 km in front of the target spacecraft, with the same transfer time. By doing these two burns in succession the chaser enters into an orbit which, in a relative sense, travels around the target spacecraft. As previously explained this is considered a natural-motion-circumnavigation (NMC) orbit. If this orbit is desired to be maintained for an extended period of time, small clean-up burns are required to avoid drift. Figure 3-5 shows a close up of the nominal trajectory during the rendezvous phase of the mission.

For Phase 3 of the mission, the results of interest will primarily be position and velocity relative navigation covariance plots, showing how accurately the chaser knows where it is with respect to the target. The next section will very briefly discuss some of the enabling technologies and aircraft and missile platforms for such a mission. Then Chapter 4 will provide the results of the simulation.

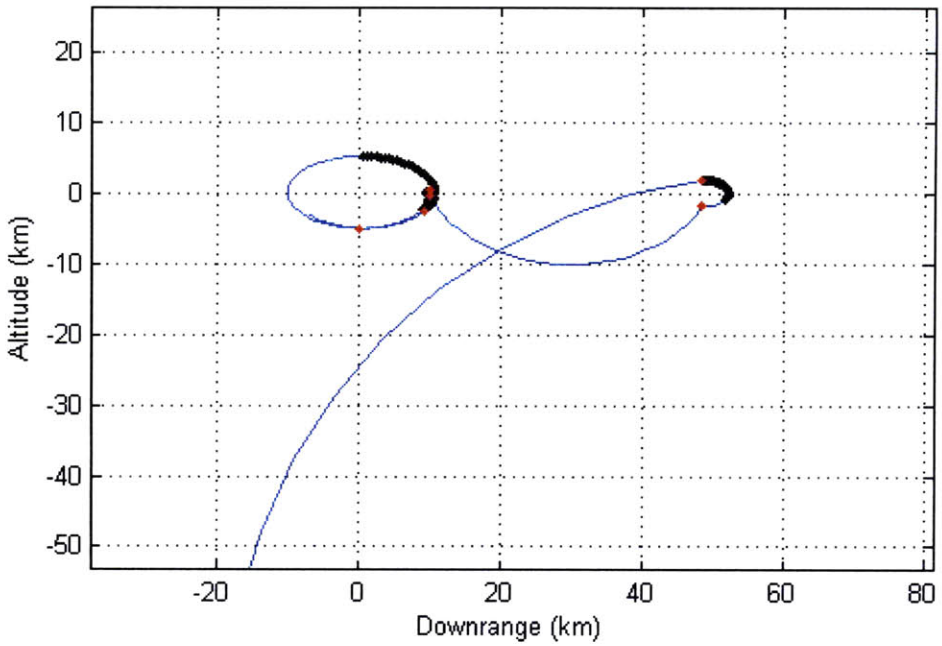

Figure 3-5: Mission Profile: Phase 3 Relative Position Plot

3.2 Spacecraft System Hardware

3.2.1 Enabling Technologies

As mentioned in the introduction, as technology allows sensors, instrumentation, and other electronics to shrink, while retaining the accuracy needed to accomplish a desired mission, smaller scale launchers will be made possible, and will be more frequently utilized. Figure 3-6 is a representation meant to show that in general as technology has been advancing for inertial-navigation-systems, their size has been getting smaller, their cost has been getting cheaper through mass-production capability of single-chip sensors, and their mean-time-between-failures (MTBF) is improving. Some of the sensors being developed and improved upon today, right here at Draper Laboratory, are Micro-Electro-Mechanical Systems (MEMS) technology. By using materials such as silicon or quartz, "MEMS offers the promise of a complete sensor and supporting electronics on a single integrated circuit chip" [8]. Figure 3-7 shows both a MEMS accelerometer on the left and a MEMS gyro on the right.

In addition to advancements in INS technology, MIT is current doing research on mi-

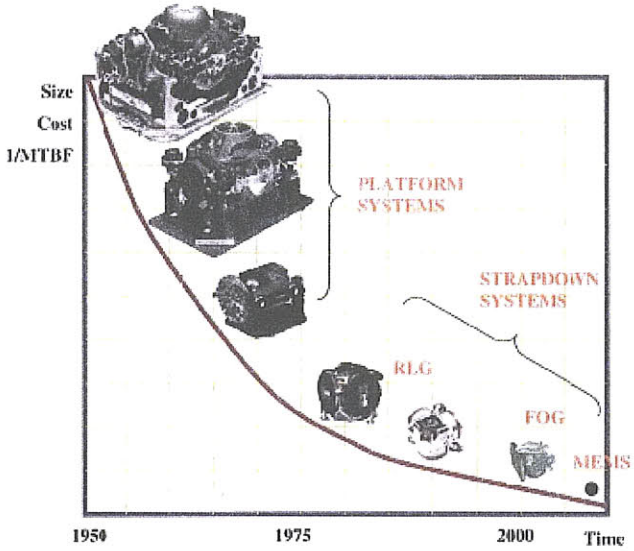

Figure 3-6: Evolution of Inertial Navigation Systems [8]

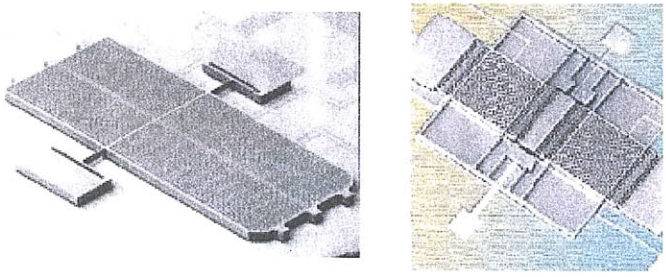

Figure 3-7: MEMS Accelerometer (left) & MEMS Gyro (right) [8]

cro rocket nozzles and micro turbopumps, printed on silicon chips. Just like the MEMS inertial systems presented about, these would have the advantage of undergoing mass production for large scale orders. Since the nozzles themselves have very low mass compared to their older generation counterparts, the thrust/weight ratio is higher. By grouping literally thousands of the nozzles together and by having independent valves for either each nozzle or for sections of nozzles, the concepts of throttleability and steerability become very real, without the mass costly gimbaled thrust vectoring systems of the past. Beyond sensors and propulsion systems, it goes beyond saying that all electronics are getting faster, smaller, and in a lot of cases require less power than older systems. All of these advances combine to open up the frontier for new systems and missions that were at one time impossible.

3.2.2 Aircraft and Missile Platforms

The goal of this program is to be able to launch a microsatellite off of an aircraft for many reasons, the most important of which are rapid deployability and mission cost deflation over traditional launches. However, as prescribed in this thesis, the requirements to launch from a high altitude and in a nose high configuration limits the type of aircraft which may accomplish this mission. Figures 3-8 and 3-9 show three jets in the US Air Force inventory which may be capable of such a feat. Both the F-15 Eagle and the F-22 Raptor have far greater thrust to weight ratios than the F-16, and are capable of accelerating while in vertical flight. The F-16 may be able to pull off a certain roll maneuver to still allow for a toss type launch of the missile, but the Eagle and the Raptor would be far superior. Originally the F-22 was only going to have internal stowage of munitions which would have made such a launch very difficult, but Congress required it to be able to be outfitted with external racks as well for more of a combined fighter/attack role. An argument could also be made that the Navy and Marine Corps F-18 Hornets would be able to accomplish this type of launch. If enough interest in the civilian sector arose for these types of launches one can envision an upstart business utilizing older, or possibly foreign built, fighter type aircraft to satisfy the need.

There would be a few benefits as well to utilizing missile sizes and casings that are

Figure 3-8: F-16 Fighting Falcon

Figure 3-9: F-15 Eagle (aft) & F-22 Raptor (fore)

already widely used in the US armed forces. A dramatic cost reduction would be possible due to already having aircraft that are outfitted to be able to carry the missile size and shape that is restructured into a rocket. As well, when an F-15 takes off with what appears to be two AIM-7 Sparrows on it no one on the ground really thinks twice, so if an enemy is keeping surveillance on our air bases they may not know exactly what type of mission the jet is taking off for. There are a few missiles in America's inventory which it may be possible to remake into small launch vehicles, two of which are pictured in Figures 3-10 and 3-11. Of course all of this still depends heavily on the continued miniaturization of technology to allow for greater payload capacity.

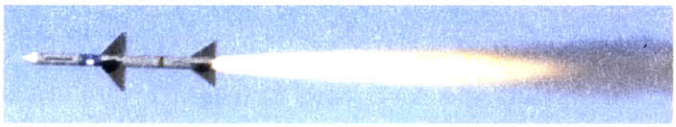

Figure 3-10: AIM-7 Sparrow Missile

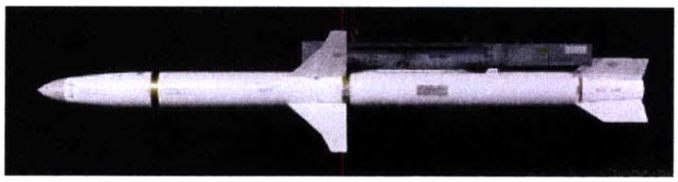

Figure 3-11: AGM-88 High-Speed Antiradiation Missile (HARM)

[This page intentionally left blank.]

Chapter 4

Application of LINCOV Tool to the Mission

4.1 Discussion of the Results

4.1.1 Phase One

Phase One takes place from launch off of a fighter aircraft until main-engine-cutoff when the spacecraft has reached a 200 km parking orbit. As discussed in Chapter 3, the nominal trajectory includes a certain wait time while at 200 km before the orbital altitude is increased to 800 km. This is done for timing considerations, and to help drive down the errors during the atmospheric part of the launch. The rockets is launched from a jet in a nose high attitude at 36,000 ft which is traveling Mach 0.8. Any number of different approximations may be made for the nominal trajectory in the atmospheric range, and it has been found that the results are more dependent on the time of flight up to 200 km as opposed to the specific approximations for the time history of the rockets flight path angle, heading, and velocity profiles. Overall, Phase 1 takes between 6.5 and 7 min. As a reminder, the rocket is assumed to have zero GPS access during the atmospheric part of the launch, as a worst-case type scenario, but the rocket is supplied with initial position and velocity information up to the modest GPS accuracy levels right at separation from the fighter. Table 4.1 provides the position and velocity navigation covariance found

	0.0	0.3	1.0	3.0	6.0	10.0
Radial (m)	0.000	308.210	1027.392	3082.383	6165.365	10276.860
Along-Track (m)	0.000	308.210	1027.392	3082.383	6165.365	10276.860
Cross-Track (m)	0.000	308.210	1027.392	3082.383	6165.365	10276.860
Radial (m/s)	0.000	3.266	10.887	32.663	65.333	108.902
Along-Track (m/s)	0.000	3.266	10.887	32.663	65.333	108.902
Cross-Track (m/s)	0.000	3.266	10.887	32.663	65.333	108.902

Table 4.1: Phase 1 Covariance versus Gyro Bias Stability

during the atmospheric part of the mission.

4.1.2 Phase Two

A large change in Phase 2 is that now the chaser spacecraft is allowed to receive updates to its position and velocity via GPS every minute. Most of the navigation errors that occurred during Phase 1 were because of errors in the IMU, and a range of IMUs were evaluated providing a range of initial covariance information for the chaser. This sets the stage for a new problem in which the active vehicle initial covariance is now a variable. In order to simulate the results of a mission in which the launch vehicle continues to fly directly to its target altitude, instead of sitting in a 200 km parking orbit for a while first, the initial wait time is driven to zero and the maneuver to increase the orbital altitude to 800 km is immediate. This is done to evaluate how well the chaser is able to navigate to SOR point number 1 with varying levels of certainty in its position and velocity at the time of the burn. The vehicle is able to begin getting GPS measurements right at the start of the mission, and the active vehicle initial covariance values are based on the simulation of the atmospheric part of the flight in Phase 1, which assumed that no GPS information was available. The values used for the active vehicle initial covariance were listed in Table 4.1.

First of all, a benchmark will be set by assuming that the IMU on the rocket is perfect thereby leaving the initial position and velocity navigation covariance at zero. By running the simulation using these assumptions, and ending it when the chaser spacecraft reaches SOR 1, the time history plots of navigation filter performances are found and are shown in Figures 4-1 and 4-2. All the error seen in these plots comes from sources outside

of the launch vehicle, such as unmodeled accelerations, maneuver error, target vehicle uncertainty, etc. Another notable value that Lincov Tools evaluates is the Δv required for the included maneuvers. In this case the total deterministic Δv required was 334.7025 m/s.

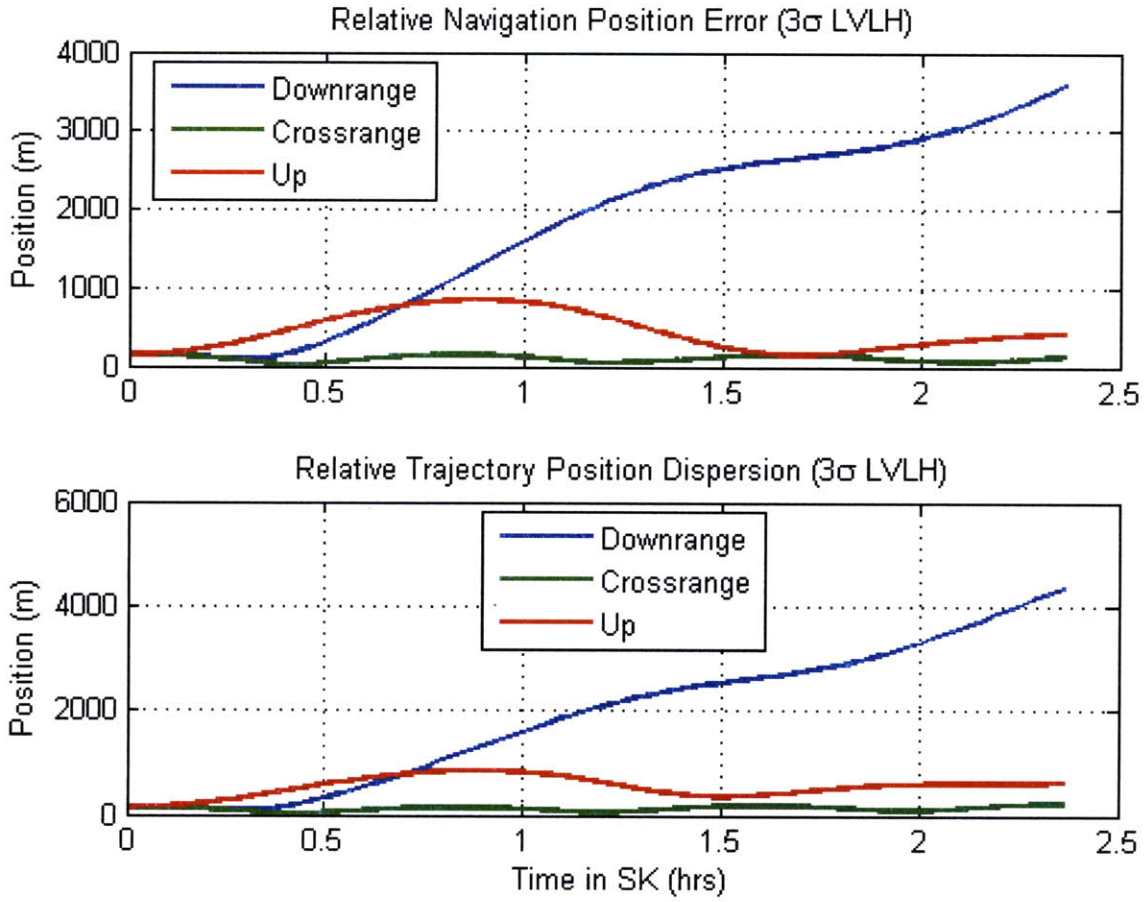

Figure 4-1: Phase 2 Position Relative Navigation Dispersion, Perfect IMU

In order to see just how much of a negative effect poor passive vehicle initial covariance has on the chaser spacecraft's ability to know its position and velocity at a future time, the results are included for the case where an IMU with a bias stability rating of 0.3 deg/hr is used aboard the rocket. During Phase 1 the navigation filter accrued 308.21 m of position uncertainty, and 3.266 m/s of velocity uncertainty. As may be seen below in Figures 4-3 and 4-4, initial covariance information is very important in keeping the spacecraft's dispersion down at acceptable levels. The upper plots on both charts are

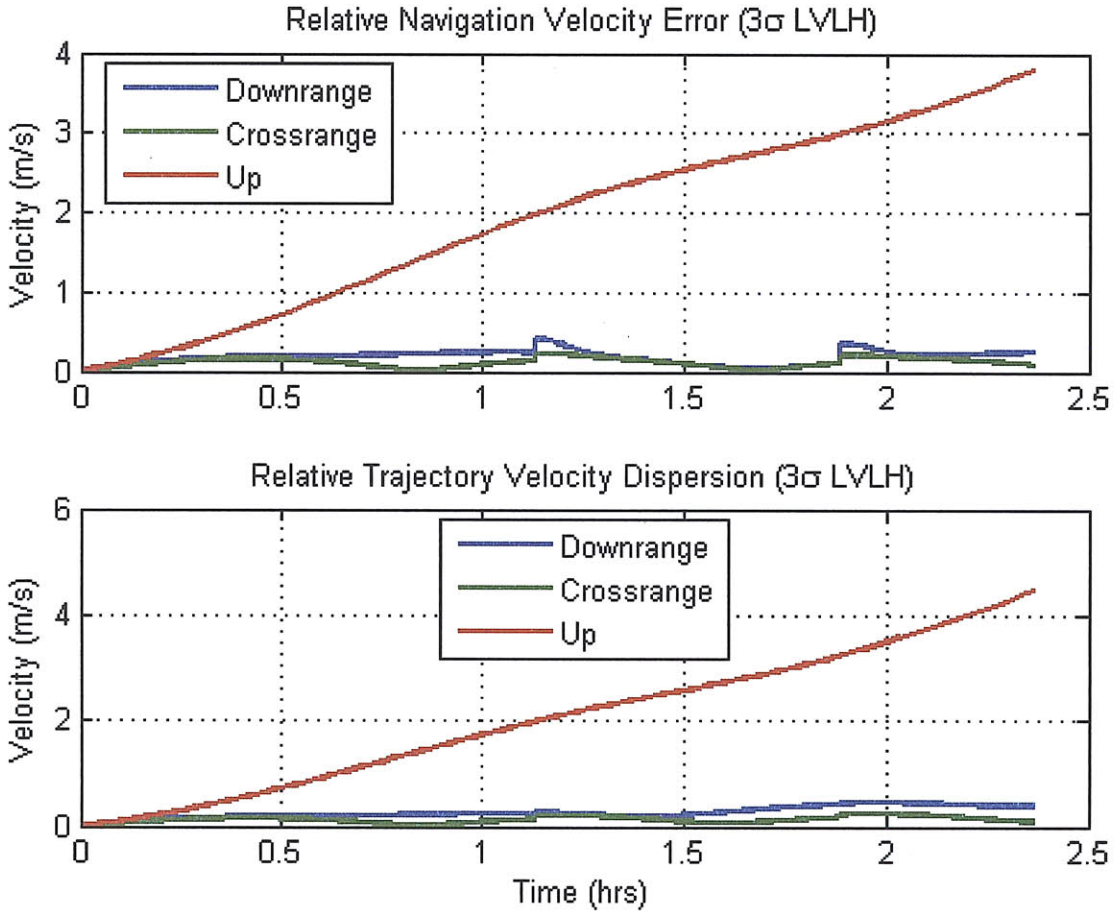

Figure 4-2: Phase 2 Velocity Relative Navigation Dispersion, Perfect IMU

relatively unchanged, due to the fact that the initial uncertainty in the chaser's state is mitigated when the GPS measurements start coming in. However the low plot diverges considerably from the perfect IMU case because the spacecraft attempts to transfer up to the 800 km orbit while its knowledge of its own position and velocity is still poor.

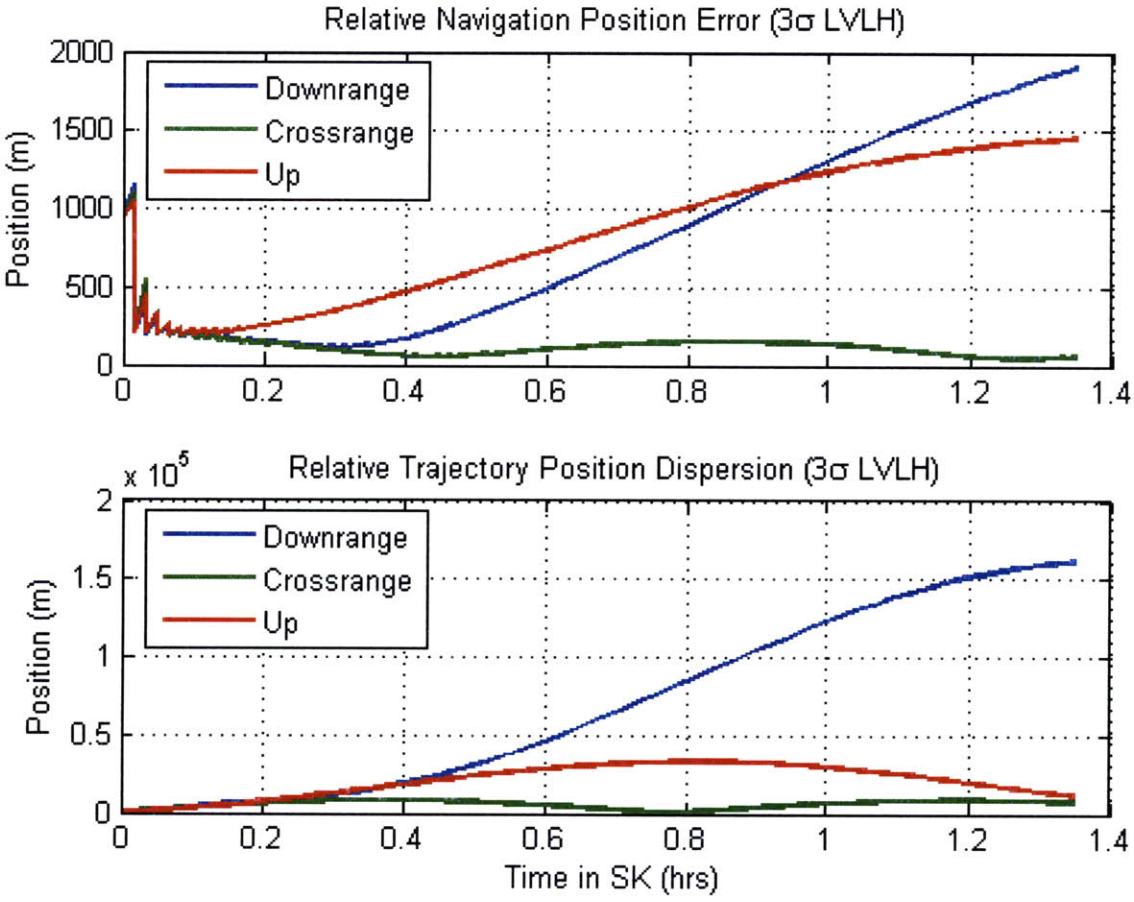

Figure 4-3: Phase 2 Position Relative Navigation Dispersion, 0.3 deg/hr IMU

The plots for the worse cases are not included here because they follow the same trends as Figures 4-3 and 4-4 did, except that the final errors in the navigation dispersion grow even more. The dispersion begins to be heavily driven by nearly only by the initial covariance of the system. Even the best case scenario of a gyro bias stability of 0.3 deg/hr gives an initial position covariance six times that obtainable from GPS, and the initial velocity covariance approximately eighty times worse. The overall navigation dispersion of these cases may be found in Tables 4.2 and 4.3. As can be seen, the errors grow quite

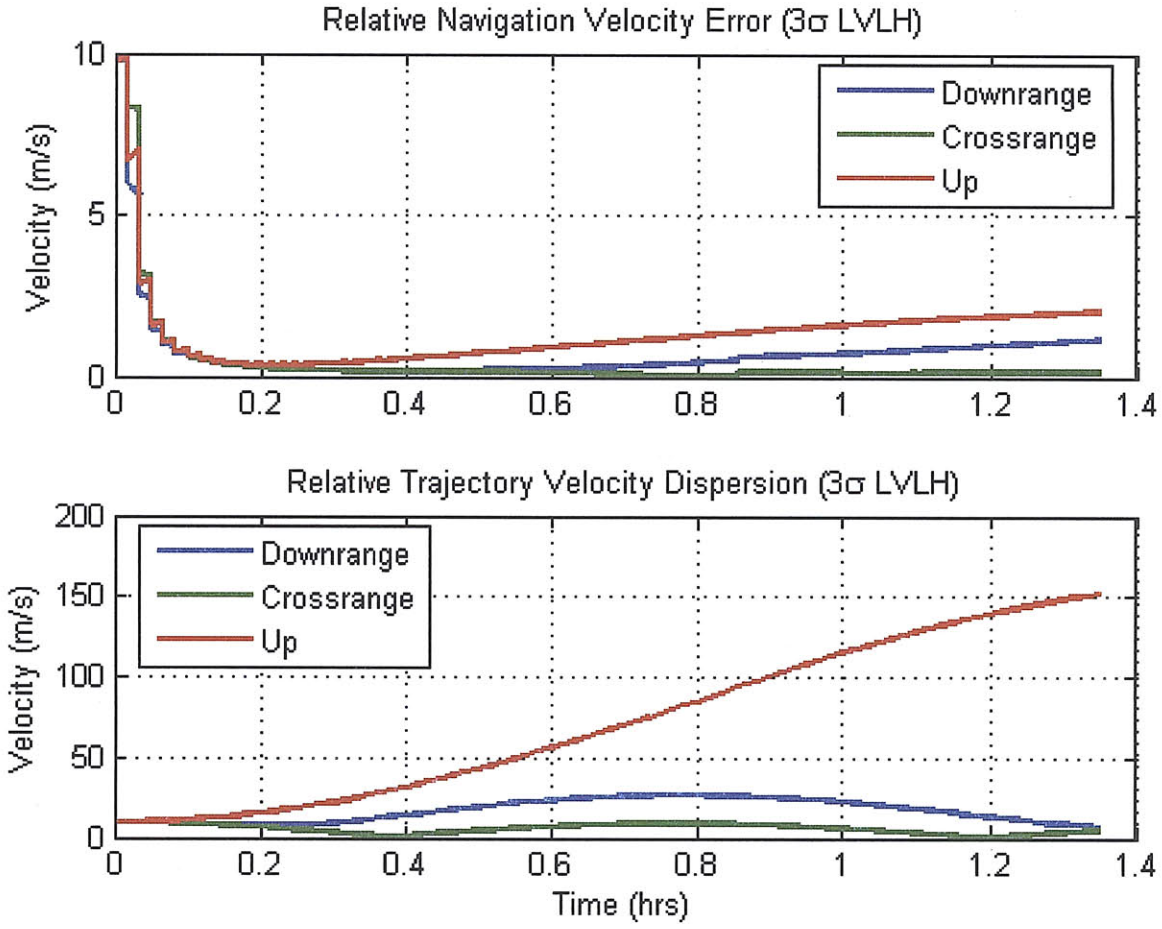

Figure 4-4: Phase 2 Velocity Relative Navigation Dispersion, 0.3 deg/hr IMU

Gyro Bias Stability (deg/hr)	Downrange	Cross-Track	Along-Track
1.0	538449	24344	38230
3.0	1615421	73034	114616
6.0	3389268	145799	245785
10.0	5385987	243503	382112

Table 4.2: Phase 2 Final Relative Position Navigation Dispersions 3σ (m)

Gyro Bias Stability (deg/hr)	Downrange	Cross-Track	Along-Track
1.0	23.3	16.7	506.5
3.0	69.9	50.1	1520
6.0	148.1	99.0	3195
10.0	233.0	166.9	5067

Table 4.3: Phase 2 Final Relative Velocity Navigation Dispersions 3σ (m/s)

quickly when the spacecraft attempts to transfer to the higher orbit with growing levels of initial state uncertainty.

One way to drive down the initial covariance of the launch vehicle before it maneuvers to raise its orbital altitude to 800 km is to allow it to receive some GPS measurements first. Since some of the initial covariance results are rather large, it does take a certain amount of time to bring the covariance down to acceptable bounds. Figures 4-5 and 4-6 show the effect on the chaser spacecraft's navigation state covariance from allowing it to sit in a parking orbit of 200 km while obtaining GPS measurements.

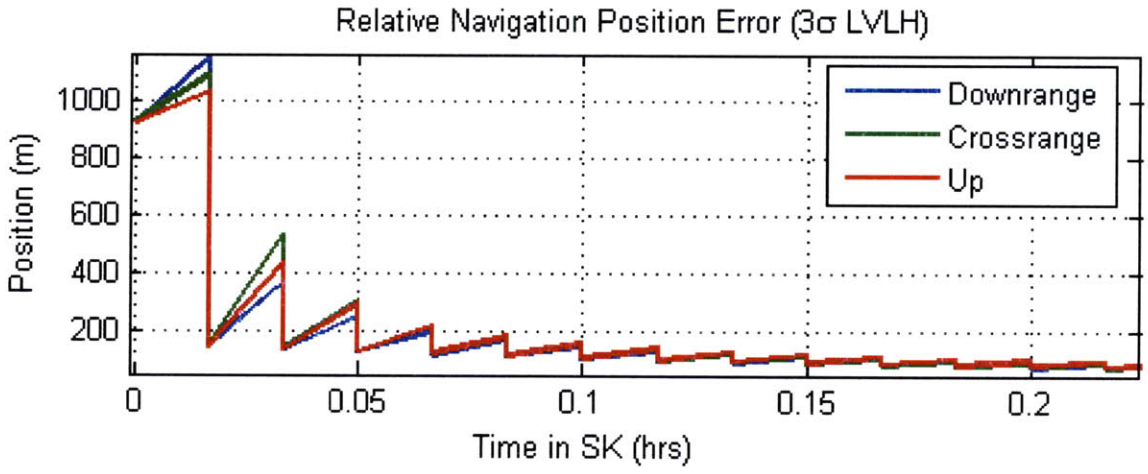

Figure 4-5: GPS Updates Effect on Position Relative Navigation Covariance, 0.3 deg/hr IMU

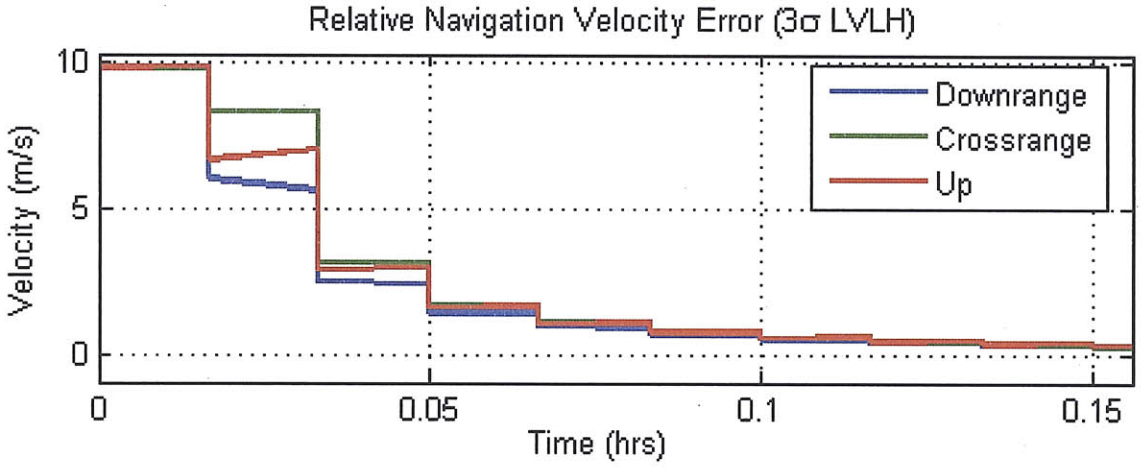

Figure 4-6: GPS Updates Effect on Velocity Relative Navigation Covariance, 0.3 deg/hr IMU

Gyro Bias Stability (deg/hr)	Measurements Needed (1 min apart)
0.3	32
1.0	36
3.0	39
6.0	42
10.0	44

Table 4.4: GPS Correction Wait Times versus Gyro Bias Stability

Table 4.4 shows approximately how long it takes for the system to drive its initial position and velocity navigation covariance down to GPS levels (50 m and 0.05 m/s) based on the rating of the onboard IMU. If the initial covariance is not reduced first, very large errors in position and velocity found in the above discussion result. Even with a good IMU (gyro bias stability of 0.3 deg/hr) the accrued error during the atmospheric part of the flight alone is too much to begin with on the trip up to 800 km.

Therefore, the nominal trajectory developed in Section 3.1.2 has enough wait time built in already to drive down errors from atmospheric launch phase and the final trajectory dispersions for Phase 2 when the spacecraft reaches SOR 1, 50 km behind the target spacecraft, is shown in Figures 4-7 and 4-8. It is found that from launch until reaching SOR 1, the chaser spacecraft knows where it is in space relative to the target vehicle within 4 km, and it has only deviated from its nominal trajectory by about 5 km. With the built in 50 km spacing between SOR 1 and the target, there is a factor of safety of 10

with the position of SOR 1 that the nominal trajectory calls for.

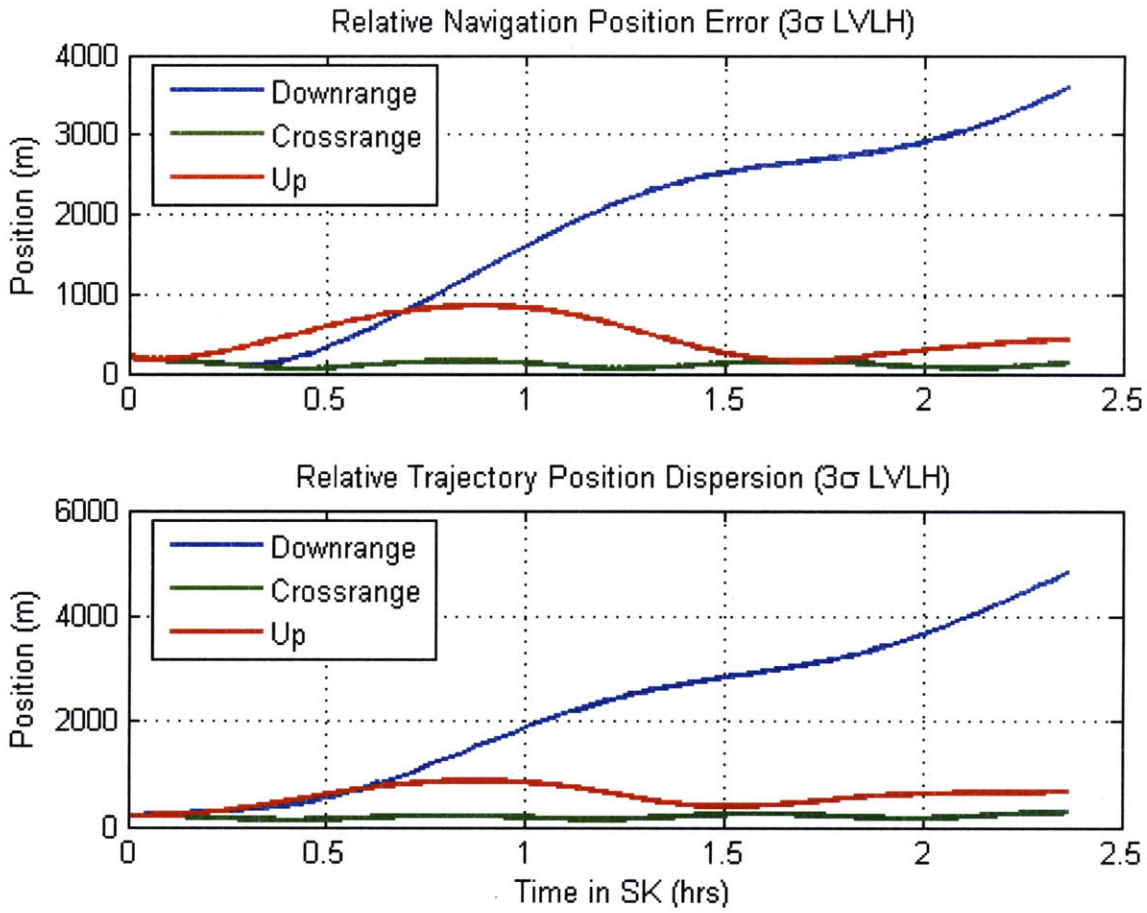

Figure 4-7: Stage 2 Position Relative Navigation Dispersion, GPS Quality Updates

4.1.3 Phase Three

This section presents results from simulations that accomplished the full mission, a combination of Phases 2 and 3. In this phase, the chaser spacecraft is attempting to navigate its way in space to the target spacecraft, according to the nominal trajectory developed in Section 3.1.2. Overall the chaser begins at a 200 km circular orbit, performs a coelliptic transfer up to an 800 km circular orbit, approximately arriving at SOR 1, 50 km downrange of the target, maneuvers to SOR 2, a position 10 km behind the target, and then enters a 10 km by 5 km football orbit around the target spacecraft. Figures 4-9 and 4-10 look at the case where the chaser spacecraft has no ability to sense its target; it simply

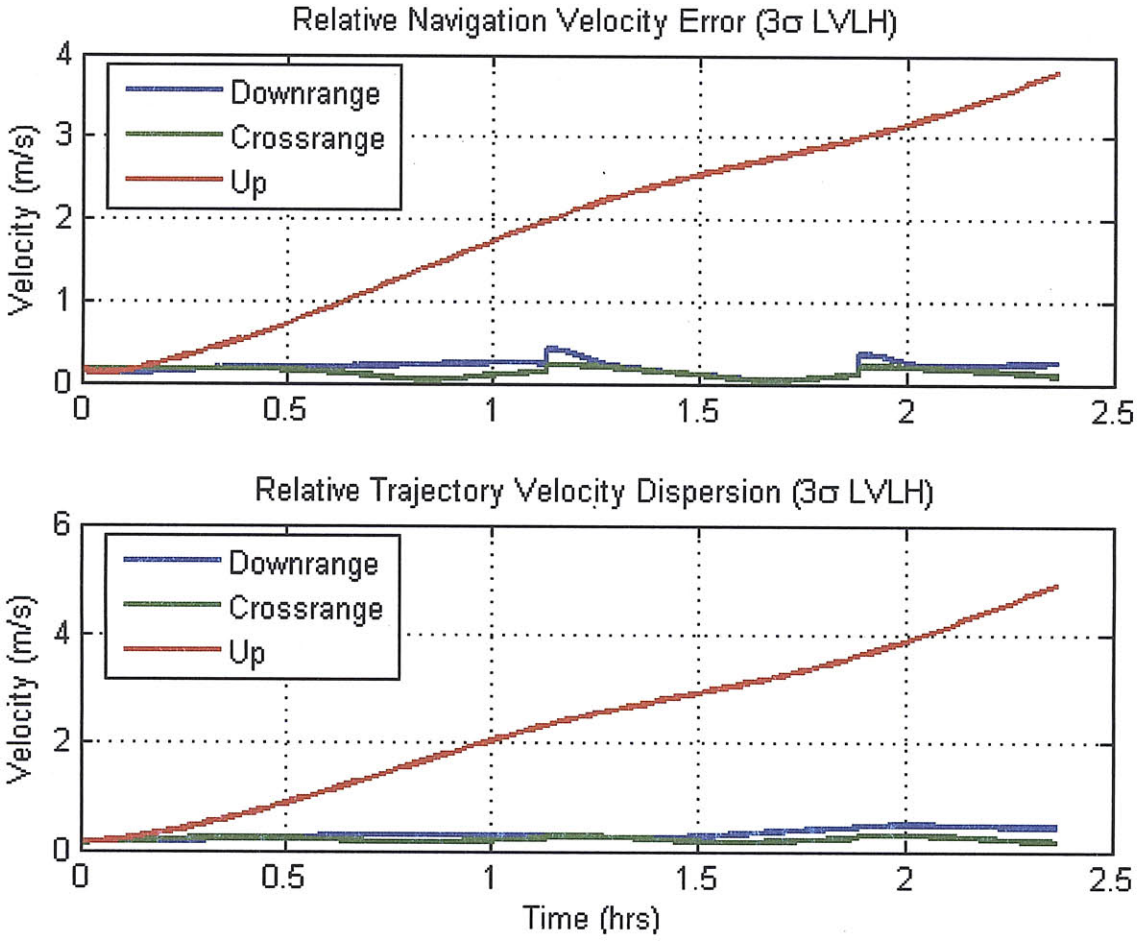

Figure 4-8: Stage 2 Velocity Relative Navigation Dispersion, GPS Quality Updates

tries to follow its nominal trajectory. While it is receiving GPS updates every minute, the relative navigation position errors continue to grow throughout the mission. This is because the error is being heavily driven by the uncertainty in the target spacecraft's position as time elapses. Since there are no updates to the target's position, in either the absolute or relative sense, this error is never reduced. As can be seen, while at the end of the mission the chaser vehicle is supposed to be in a 10 km by 5 km football orbit around the target, it only knows the position of the target within approximately 10 km, which undoubtedly is a dangerous situation. The spacecraft needs to have better knowledge of its target in order to perform its maneuvers correctly to enter into a safe relative orbit.

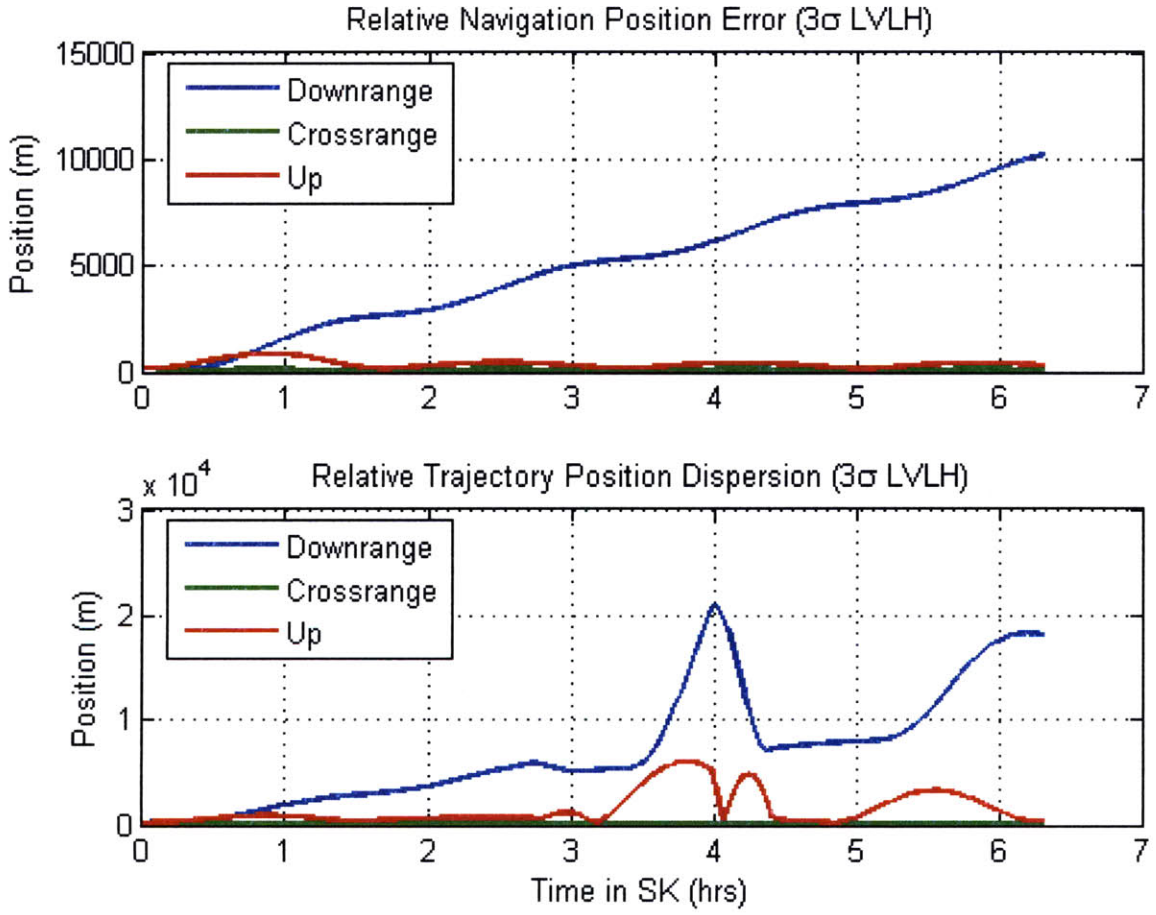

Figure 4-9: Phase 3 Position Navigation Filter Plots, No Optical Camera

A second simulation shows the effectiveness of relative sensing on rendezvous operations. Nothing is changed for this run with the exception of the addition of an optical

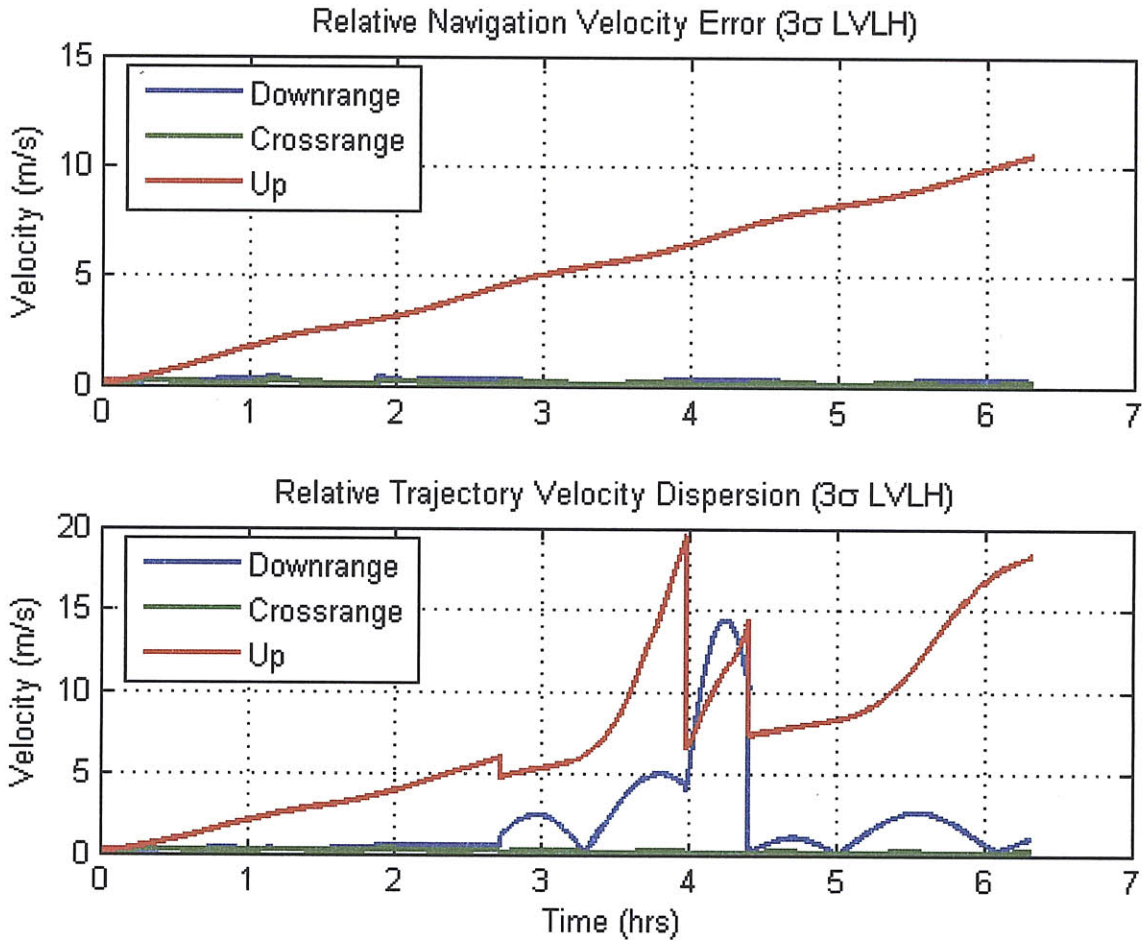

Figure 4-10: Phase 3 Velocity Navigation Filter Plots, No Optical Camera

camera. This camera is only used for targeting the target spacecraft by detecting its angular position from the chaser spacecraft; it does not sense range at all. As previously mentioned, Lincov Tools allows for the estimation of range from an optical sensor, but that functionality is not included in these results, and in either case that ability requires ranges closer than this mission ever approaches. The camera is tuned so that it can begin detecting the target spacecraft from a range of 70 km. As may be seen in Figures 4-11 and 4-12, the relative covariance between the spacecraft is greatly reduced, beginning at around 1.75 hrs, which is when the spacecraft begin to be close enough together for the relative sensor to be functional. One important mission parameter to be noted, however, is that this type of sensing is dependent on the lighting conditions of the spacecraft. If the target is currently in the eclipse of the earth then an optical sensor is going to be ineffective unless an artificial light source is being generated on the target vehicle. Other types of relative measurements may be possible during eclipse, such as LIDAR measurements, but for the sake of this research it is assumed that the mission can be designed in such a way that all maneuvers may be performed in a lighted condition.

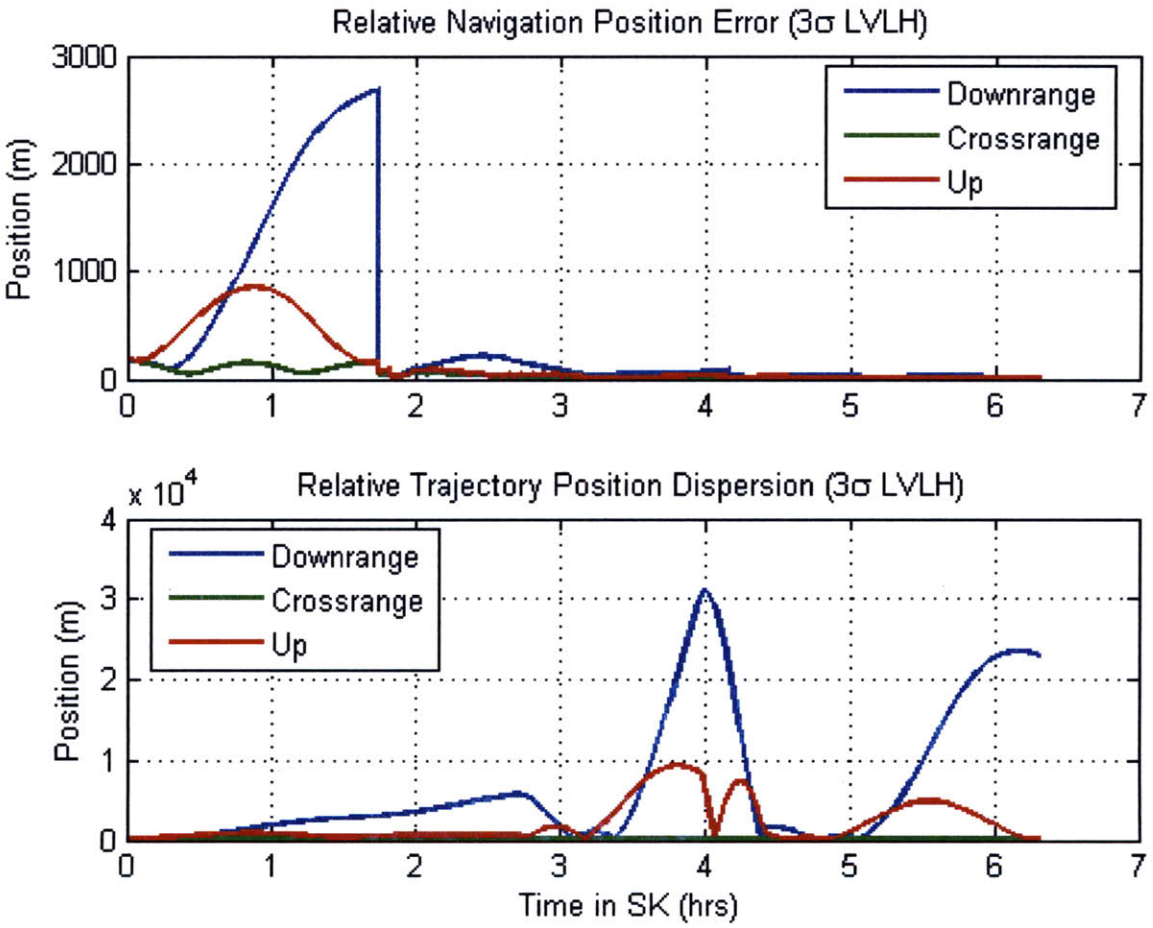

Figure 4-11: Phase 3 Position Navigation Filter Plots, With Optical Camera

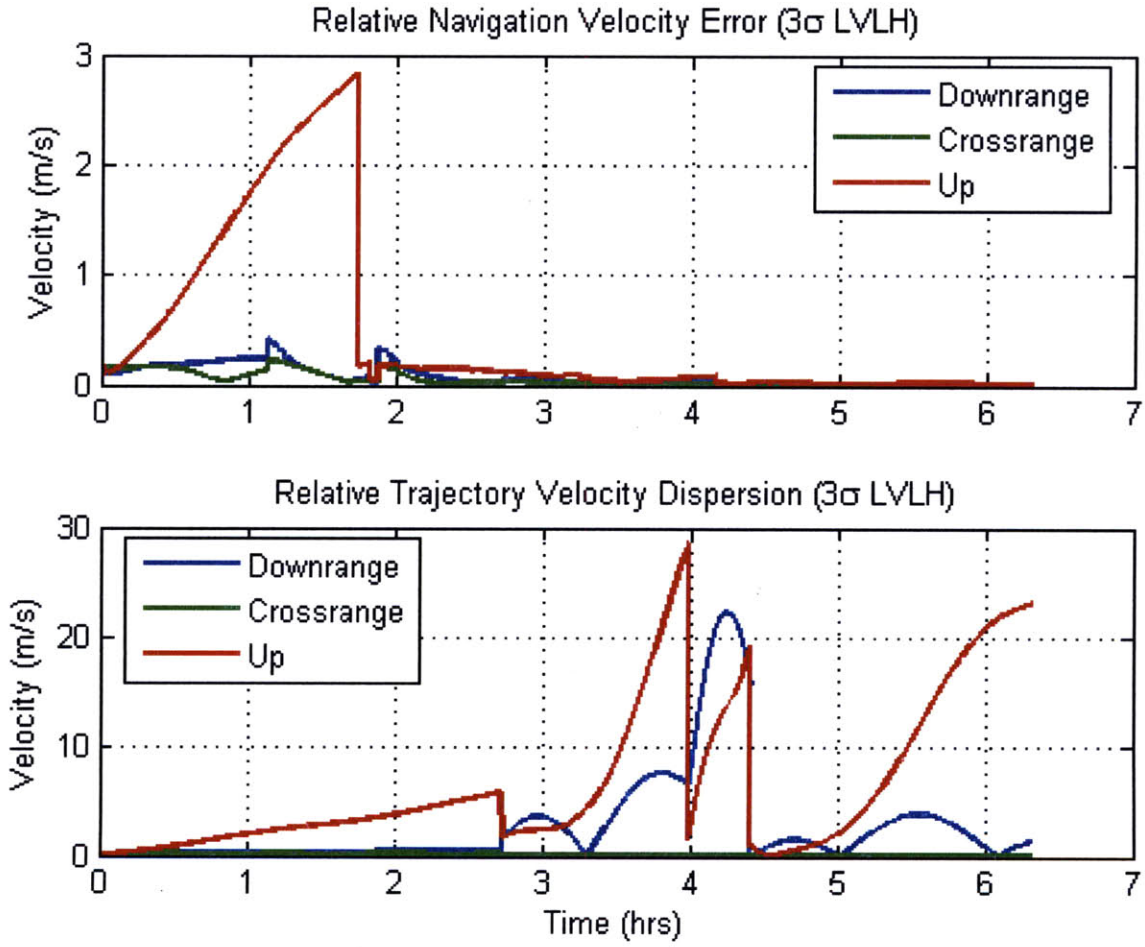

Figure 4-12: Phase 3 Velocity Navigation Filter Plots, With Optical Camera

[This page intentionally left blank.]

Chapter 5

Conclusions

In summary, Linear Covariance Analysis is a useful tool for estimating the capability of a space system which leads to a better understanding of spacecraft and mission design parameters. It was seen that measurements, whether they be GPS, relative measurements using an optical camera, or otherwise, improve the overall position and velocity navigation covariance of a spacecraft. In addition, maneuvers performed by the spacecraft help to drive down its navigation dispersion and allow it to better follow a nominal trajectory.

For missions where one is concerned with how accurately a launch vehicle can place a spacecraft into a target orbit, it is important that the launch vehicle has enough sensing ability to know its current position and velocity well enough as to not go completely off course, and it appears that long periods of time without some type of position and velocity update can lead to large errors at the tail-end of the mission. By simply allowing a GPS capable spacecraft time for additional measurements to better estimate its absolute position and velocity, large maneuvers will not be completely disastrous to the overall mission. If a spacecraft must perform rendezvous or near-rendezvous operations it is absolutely essential that the chaser spacecraft has some way of sensing its target, either though the use of an optical camera, LIDAR, cooperation from the target itself, etc. Without these types of measurements the chaser does not know the position of the target well enough to navigate accurately and safely into position.

The continuing advancements of technology are driving down the size and cost of sensors and other electronics used in space missions, and eventually will enable more

possibilities when it comes to the effective utilization of space. Smaller launch vehicles, which will be highly responsive and globally deployable, will be able to accomplish more with less, and the nations and corporations which grasp these new capabilities will be a step ahead of the rest.

Appendix A

More Detailed Mathematical Background to LINCOV

This chapter summarizes the information presented in Section 2.2 and expands on it to show how the navigation filters matrices are partitioned. The development of the navigation filters found here is from David Geller's work [2]. The navigation state and covariance propagation algorithms are found in Equations A.1 and A.2.

$$\dot{\hat{\mathbf{x}}} = \hat{\mathbf{f}}(\hat{\mathbf{x}}, \hat{\mathbf{u}}, \tilde{\mathbf{y}}, t) \tag{A.1}$$

$$\dot{\hat{P}} = \left[\hat{F}_{\hat{x}} + \hat{F}_{\tilde{y}}\hat{C}_{\hat{x}}\right]\hat{P} + \hat{P}\left[\hat{F}_{\hat{x}} + \hat{F}_{\tilde{y}}\hat{C}_{\hat{x}}\right]^T + \hat{F}_{\tilde{y}}\hat{S}_{\eta}\hat{F}_{\tilde{y}}^T + \hat{S}_w \tag{A.2}$$

The navigation state vector $\hat{\mathbf{x}}$ is a truncated version of the true state $\mathbf{x}$, as explained in Equation A.3.

$$\hat{\mathbf{x}} = C_{\hat{n}\times n}\mathbf{x} \tag{A.3}$$

The Kalman gain used during this development is found in Equation A.4.

$$\hat{K}(t_k) = \hat{P}(t_k)\hat{H}_{\hat{x}}^T(t_k)\left[\hat{H}_{\hat{x}}(t_k)\hat{P}(t_k)\hat{H}_{\hat{x}}^T(t_k) + \hat{R}_{\nu}(t_k)\right]^{-1} \tag{A.4}$$

The navigation state and state covariance update algorithms come from the Joseph

formulation and are found in Equations A.5 and A.6.

$$\hat{\mathbf{x}}_k^+ = \hat{\mathbf{x}}_k^- + \hat{K}(t_k)[\hat{\mathbf{z}}_k - \hat{\mathbf{h}}(\hat{\mathbf{x}}_k, t_k)] \tag{A.5}$$

$$\hat{P}(t_k^+) = \left[I - \hat{K}(t_k)\hat{H}_{\hat{x}}(t_k)\right] \hat{P}(t_k^-) \left[I - \hat{K}(t_k)\hat{H}_{\hat{x}}(t_k)\right]^T + \hat{K}(t_k)\hat{R}_\nu(t_k)\hat{K}^T(t_k) \tag{A.6}$$

Once the navigation state and state covariance are updated, the algorithm to correct them is found in Equations A.7 and A.8.

$$\hat{\mathbf{x}}_j^{+c} = \hat{\mathbf{x}}_j^{-c} + \hat{\mathbf{d}}(\hat{\mathbf{x}}^{-c}, \boldsymbol{\Delta}\hat{\mathbf{u}}, \boldsymbol{\Delta}\tilde{\mathbf{y}}, t_j) \tag{A.7}$$

$$\begin{aligned}\hat{P}(t_j^{+c}) = \left[I + \hat{D}_{\hat{x}}(t_j) + \hat{D}_{\Delta\tilde{y}}(t_j)\Delta\hat{C}_{\hat{x}}(t_j)\right] \hat{P}^{-c}(t_j) \left[I + \hat{D}_{\hat{x}}(t_j) + \hat{D}_{\Delta\tilde{y}}(t_j)\Delta\hat{C}_{\hat{x}}(t_j)\right]^T \\ + \hat{D}_{\Delta\tilde{y}}(t_j)\hat{S}_{\Delta\eta}\hat{D}_{\Delta\tilde{y}}(t_j)^T + \hat{S}_{\Delta w}(t_j)\end{aligned} \tag{A.8}$$

The pointing, maneuver targeting, and control algorithms, shown in Equations A.9 and A.10, are used to generate actuator commands $\hat{\mathbf{u}}$ and $\Delta\hat{\mathbf{u}}(t_j)$.

$$\hat{\mathbf{u}} = \hat{\mathbf{g}}(\hat{\mathbf{x}}, t) \tag{A.9}$$

$$\boldsymbol{\Delta}\hat{\mathbf{u}}(t_j) = \boldsymbol{\Delta}\hat{\mathbf{g}}(\hat{\mathbf{x}}_j^{-c}, t_j) \tag{A.10}$$

The above equations are then linearized about the nominal trajectory, $\bar{\mathbf{x}}(t)$, to provide a time history of the navigation dispersions from nominal and state dispersions. This is begun in Equations A.11 and A.12.

$$\delta\dot{\mathbf{x}} = F_x\delta\mathbf{x} + F_{\hat{u}}\hat{G}_{\hat{x}}\delta\hat{\mathbf{x}} + \mathbf{w} \tag{A.11}$$

$$\delta\dot{\hat{\mathbf{x}}} = (\hat{F}_{\hat{x}} + \hat{F}_{\hat{u}}\hat{G}_{\hat{x}})\delta\hat{\mathbf{x}} + \hat{F}_{\tilde{y}}C_x\delta\mathbf{x} + \hat{F}_{\tilde{y}}\eta \tag{A.12}$$

The state update and measurement equations are then linearized to produce Equations A.13 and A.14.

$$\delta \mathbf{x}_k^+ = \delta \mathbf{x}_k^- \tag{A.13}$$

$$\delta \hat{\mathbf{x}}_k^+ = \hat{K}(t_k) H_x(t_k) \delta \mathbf{x}_k^- + \left[I - \hat{K}(t_k) \hat{H}_{\hat{x}}(t_k) \right] \delta \hat{\mathbf{x}}_k^- + \hat{K}(t_k) \nu_k \tag{A.14}$$

Next the state corrections are linearized to produce Equations A.15 and A.16.

$$\delta \mathbf{x}_j^{+c} = \left[I + D_x(t_j) \right] \delta \mathbf{x}_j^{-c} + D_{\Delta \hat{u}}(t_j) \Delta \hat{G}_{\hat{x}}(t_j) \delta \hat{\mathbf{x}}_j^{-c} + \mathbf{\Delta w}_j \tag{A.15}$$

$$\delta \hat{\mathbf{x}}_j^{+c} = \left[I + \hat{D}_{\hat{x}}(t_j) + \hat{D}_{\Delta \hat{u}}(t_j) \Delta \hat{G}_{\hat{x}}(t_j) \right] \delta \hat{\mathbf{x}}_j^{-c} + \hat{D}_{\Delta \tilde{y}}(t_j) \Delta C_x(t_j) \delta \mathbf{x}_j^{-c} + \hat{D}_{\Delta \tilde{y}}(t_j) \mathbf{\Delta} \eta_j \tag{A.16}$$

The true dispersions and the navigated dispersions are then combined into one state vector which will simply be called $\mathbf{X}$.

$$\mathbf{X} = \begin{bmatrix} \delta \mathbf{x} \\ \delta \hat{\mathbf{x}} \end{bmatrix} \tag{A.17}$$

How well the chaser spacecraft is able to follow the nominal trajectory is seen by evaluating the covariance of the true trajectory dispersions, D, as in Equation A.18. Similarly, navigation performance is seen in the covariance of the true navigation errors P_{true}, as in Equation A.19.

$$D = E\left[\delta \mathbf{x}(t) \delta \mathbf{x}^T(t) \right] = \left(I_{n \times n} \;\; 0_{n \times \hat{n}} \right) P_x \begin{pmatrix} I_{n \times n} \\ 0_{\hat{n} \times n} \end{pmatrix} \tag{A.18}$$

$$P_{true} = E\left[\left\{ \delta \hat{\mathbf{x}}(t) - C \delta \mathbf{x}(t) \right\} \left\{ \delta \hat{\mathbf{x}}(t) - C \delta \mathbf{x}(t) \right\}^T \right] = \left(-C_{\hat{n} \times n} \;\; I_{\hat{n} \times \hat{n}} \right) P_x \begin{pmatrix} -C_{n \times \hat{n}}^T \\ I_{\hat{n} \times \hat{n}} \end{pmatrix} \tag{A.19}$$

Full models of the dynamics, including gravitational forces and torques, atmospheric forces and torques, actuators, gyros, star-cameras (not used in this thesis), and optical tracking cameras, are developed, and then converted to flight software models by limiting the number of states to $\hat{n}$ from the full-model of n states. The navigation state is defined by Equation A.20.

$$\hat{\mathbf{x}} = (\hat{\mathbf{x}}_o, \hat{\mathbf{x}}_c, \hat{\mathbf{p}})^T \tag{A.20}$$

This state vector is made up of 13 states for the target spacecraft, 10 for the chaser spacecraft, and 24 parameter states, shown in Equations A.21 to A.23.

$$\hat{\mathbf{x}}_o = (\hat{\mathbf{r}}_o^i, \hat{\mathbf{v}}_o^i, \hat{\mathbf{q}}_o^i, \hat{\omega}_o^o)^T \tag{A.21}$$

$$\hat{\mathbf{x}}_c = (\hat{\mathbf{r}}_c^i, \hat{\mathbf{v}}_c^i, \hat{\mathbf{q}}_c^i)^T \tag{A.22}$$

$$\hat{\mathbf{p}} = (\hat{\mathbf{p}}_{gyro}, \hat{\mathbf{p}}_{optrk}, \hat{\mathbf{p}}_{\Delta v})^T \tag{A.23}$$

The navigation state propagation algorithm is shown in Equations A.24 to A.26, while the variables are explained in Equations A.27 to A.34.

$$\dot{\hat{\mathbf{x}}}_o = \hat{\mathbf{f}}_o(\hat{\mathbf{x}}_o) \tag{A.24}$$

$$\dot{\hat{\mathbf{x}}}_c = \hat{\mathbf{f}}_c(\hat{\mathbf{x}}_c, \hat{\mathbf{u}}, \tilde{\mathbf{y}}) \tag{A.25}$$

$$\dot{\hat{\mathbf{p}}} = \hat{\mathbf{f}}_p(\hat{\mathbf{p}}) \tag{A.26}$$

$$\dot{\hat{\mathbf{r}}}_o^i = \hat{\mathbf{v}}_o^i \tag{A.27}$$

$$\dot{\hat{\mathbf{v}}}_o^i = \hat{\mathbf{F}}_{grav_o}^i(\hat{\mathbf{r}}_o^i)/\hat{m}_o \tag{A.28}$$

$$\dot{\hat{\mathbf{q}}}_o^i = \frac{1}{2}\hat{\omega}_o^o \otimes \hat{\mathbf{q}}_o^i \tag{A.29}$$

$$\dot{\hat{\omega}}_o^o = \hat{I}_o^{-1}\left[\hat{\mathbf{T}}_{grav_o}^o(\hat{\mathbf{r}}_o^i, \hat{\mathbf{q}}_o^i) - \hat{\omega}_o^o \times \hat{I}_o\hat{\omega}_o^o\right] \tag{A.30}$$

$$\dot{\hat{\mathbf{r}}}_c^i = \hat{\mathbf{v}}_c^i \tag{A.31}$$

$$\dot{\hat{\mathbf{v}}}_c^i = \hat{\mathbf{F}}_{grav_c}^i(\hat{\mathbf{r}}_c^i)/\hat{m}_c \tag{A.32}$$

$$\dot{\hat{\mathbf{q}}}_c^i = \frac{1}{2}(\tilde{\omega}_c^c + \hat{\mathbf{g}}_{comp}) \otimes \hat{\mathbf{q}}_c^i \tag{A.33}$$

$$\dot{\hat{p}}_i = -\frac{\hat{p}_i}{\hat{\tau}_i},\ i = 1, 2, 3, ..., \hat{n}_p \tag{A.34}$$

As stated earlier in this appendix, the navigations state covariance propagation equation is found again in Equation A.35.

$$\dot{\hat{P}} = \left[\hat{F}_{\hat{x}} + \hat{F}_{\tilde{y}}\hat{C}_{\hat{x}}\right]\hat{P} + \hat{P}\left[\hat{F}_{\hat{x}} + \hat{F}_{\tilde{y}}\hat{C}_{\hat{x}}\right]^T + \hat{F}_{\tilde{y}}\hat{S}_\eta\hat{F}_{\tilde{y}}^T + \hat{S}_w \tag{A.35}$$

The matrices contained in Equation A.35 are described more fully in Equations A.36 to A.40, and are further broken down into more matrix partitions in Equations A.41 to A.44.

$$\hat{S}_\eta = \hat{S}_{\eta_{gyro}} \tag{A.36}$$

$$\hat{C}_{\hat{x}} = \frac{\partial\tilde{\omega}_c^c}{\partial\hat{\mathbf{x}}} = \begin{pmatrix} 0_{3\times12} & 0_{3\times9} & -\partial\tilde{\omega}_c^c/\partial\hat{\mathbf{p}}_{gyro} & 0_{3\times3} & 0_{3\times3} & 0_{3\times9} \end{pmatrix} \tag{A.37}$$

$$\hat{F}_{\tilde{y}} = \frac{\partial\hat{\mathbf{f}}}{\partial\tilde{\omega}_c^c} = \begin{pmatrix} 0_{3\times12} & 0_{3\times6} & I_{3\times3} & 0_{3\times24} \end{pmatrix} \tag{A.38}$$

$$\hat{S}_w = \begin{pmatrix} \hat{S}_{w_o} & 0_{12\times9} & 0_{12\times24} \\ 0_{9\times12} & \hat{S}_{w_c} & 0_{9\times24} \\ 0_{24\times12} & 0_{24\times9} & -Diag([\hat{\sigma}_{p_1}^2, \hat{\sigma}_{p_2}^2, ..., \hat{\sigma}_{p_24}^2]) \end{pmatrix} \tag{A.39}$$

$$\hat{F}_{\hat{x}} = \frac{\partial\hat{\mathbf{f}}}{\partial\hat{\mathbf{x}}} = \begin{pmatrix} \partial\hat{\mathbf{f}}_o/\partial\hat{\mathbf{x}}_o & 0_{12\times9} & 0_{12\times24} \\ 0_{9\times12} & \partial\hat{\mathbf{f}}_c/\partial\hat{\mathbf{x}}_c & 0_{9\times24} \\ 0_{24\times12} & 0_{24\times9} & -Diag([\frac{1}{\hat{\tau}_1}, \frac{1}{\hat{\tau}_2}, ..., \frac{1}{\hat{\tau}_{24}}]) \end{pmatrix} \tag{A.40}$$

$$\hat{S}_{w_o} = \begin{pmatrix} 0_{3\times3} & 0_{3\times3} & 0_{3\times3} & 0_{3\times3} \\ 0_{3\times3} & \hat{S}_{w_{grav}} + \hat{S}_{w_{aero}}^o & 0_{3\times3} & 0_{3\times3} \\ 0_{3\times3} & 0_{3\times3} & 0_{3\times3} & 0_{3\times3} \\ 0_{3\times3} & 0_{3\times3} & 0_{3\times3} & \sigma_{\hat{\omega}}^2 I_{3\times3} \end{pmatrix} \tag{A.41}$$

$$\hat{S}_{w_c} = \begin{pmatrix} 0_{3\times3} & 0_{3\times3} & 0_{3\times3} \\ 0_{3\times3} & \hat{S}_{w_grav} + \hat{S}^c_{w_{aero}} & 0_{3\times3} \\ 0_{3\times3} & 0_{3\times3} & 0_{3\times3} \end{pmatrix} \tag{A.42}$$

$$\partial\hat{\mathbf{f}}_o/\partial\hat{\mathbf{x}}_o = \begin{pmatrix} 0_{3\times3} & I_{3\times3} & 0_{3\times3} & 0_{3\times3} \\ \hat{m}_o^{-1}\partial\mathbf{F}^i_{grav_o}/\partial\hat{\mathbf{r}}^i_o & 0_{3\times3} & 0_{3\times3} & 0_{3\times3} \\ 0_{3\times3} & 0_{3\times3} & -[\hat{\omega}^o_o\times] & I_{3\times3} \\ \hat{I}_o^{-1}\partial\mathbf{T}^o_{grav_o}/\partial\hat{\mathbf{r}}^i_o & 0_{3\times3} & \hat{I}_o^{-1}\partial\mathbf{T}^o_{grav_o}/\partial\hat{\theta}^o_o & \{[(I_o\hat{\omega}^o_o)\times] - [\hat{\omega}^o_o\times]I_o\} \end{pmatrix} \tag{A.43}$$

$$\partial\hat{\mathbf{f}}_c/\partial\hat{\mathbf{x}}_c = \begin{pmatrix} 0_{3\times3} & I_{3\times3} & 0_{3\times3} \\ \hat{m}_c^{-1}\partial\mathbf{F}^i_{grav_c}/\partial\hat{\mathbf{r}}^i_c & 0_{3\times3} & 0_{3\times3} \\ 0_{3\times3} & 0_{3\times3} & -[(\tilde{\omega}^c_c + \hat{\mathbf{g}}_{comp})\times] \end{pmatrix} \tag{A.44}$$

Appendix B

Presentation of Additional Results and Test Cases

The following plots are labeled according to what they are showing, and were omitted in the main text of the thesis for relevance and continuity reasons. The important information obtained from these plots has already been reported in tabular format within the main thesis, in Section 4.1.2.

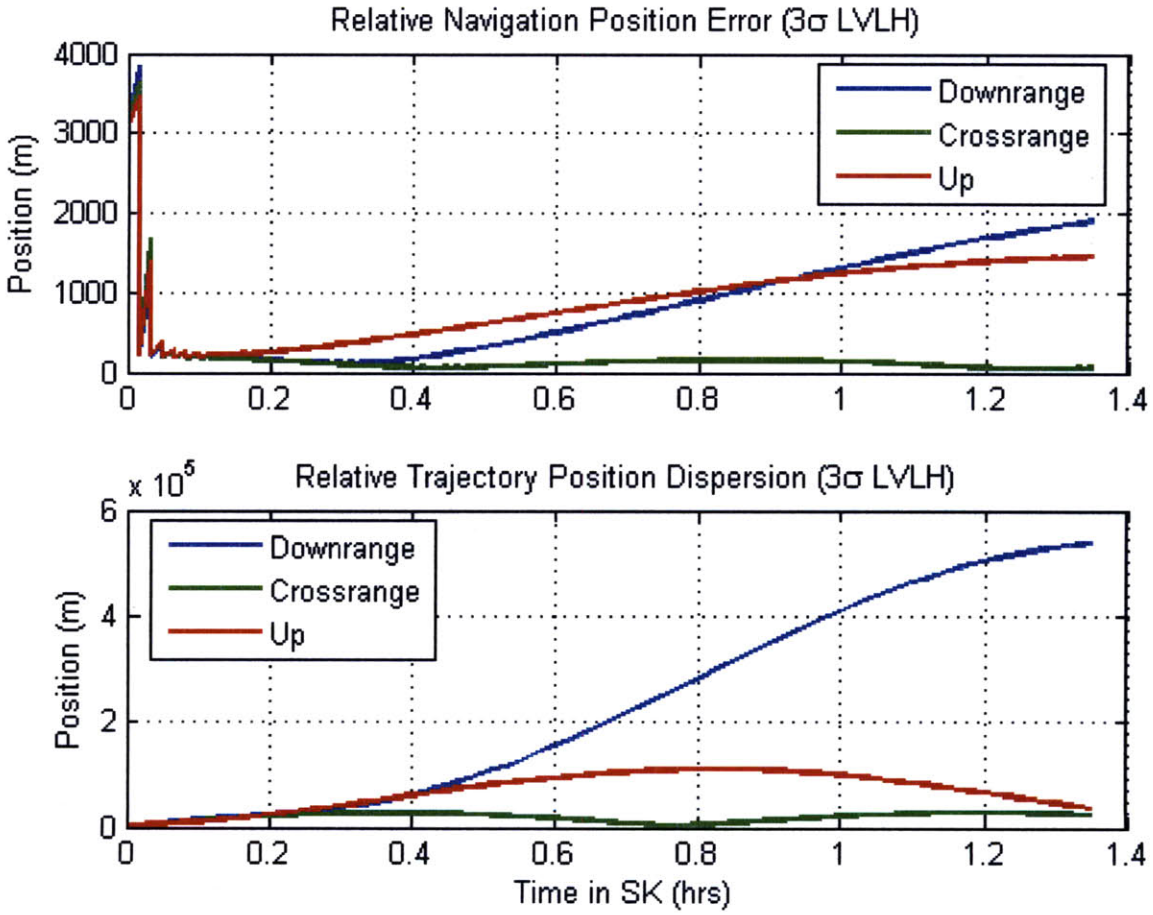

Figure B-1: Phase 2 Position Relative Navigation Dispersion, 1.0 deg/hr IMU

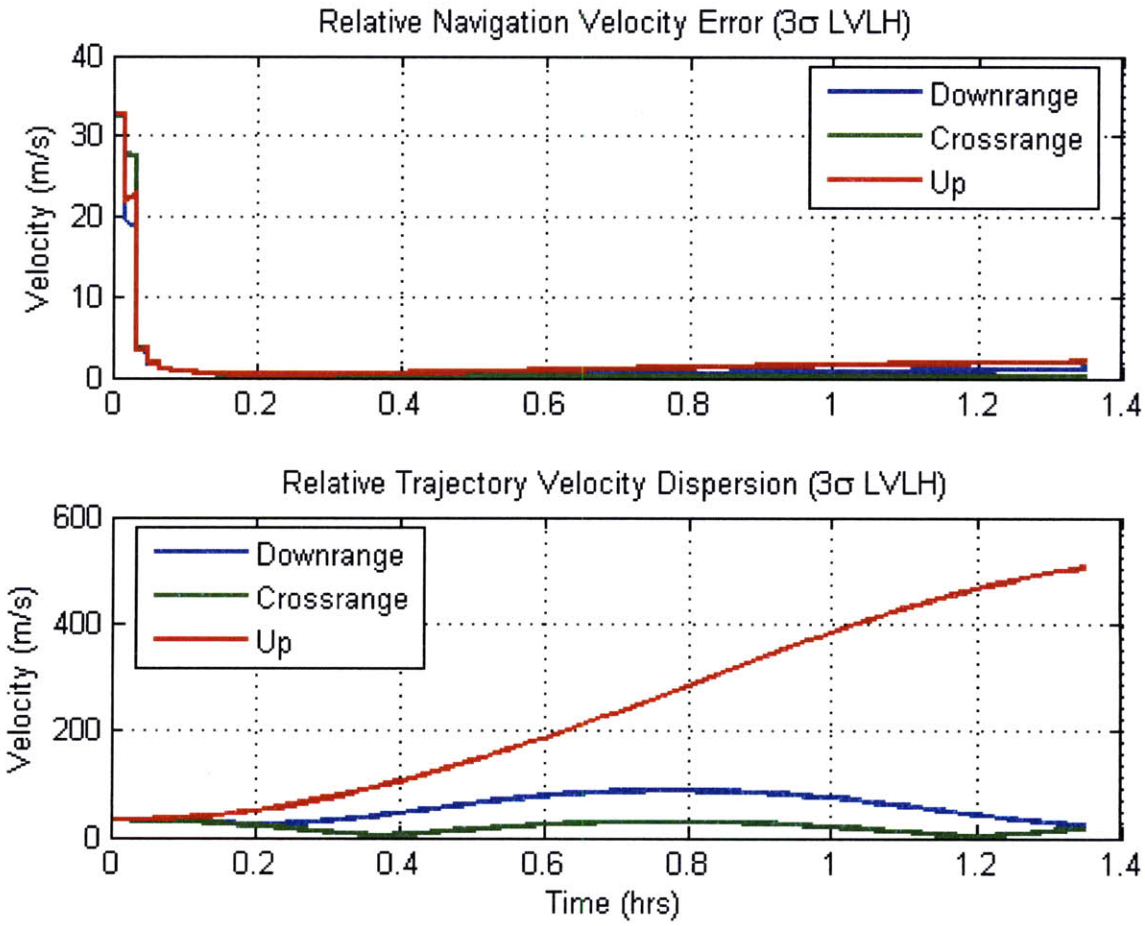

Figure B-2: Phase 2 Velocity Relative Navigation Dispersion, 1.0 deg/hr IMU

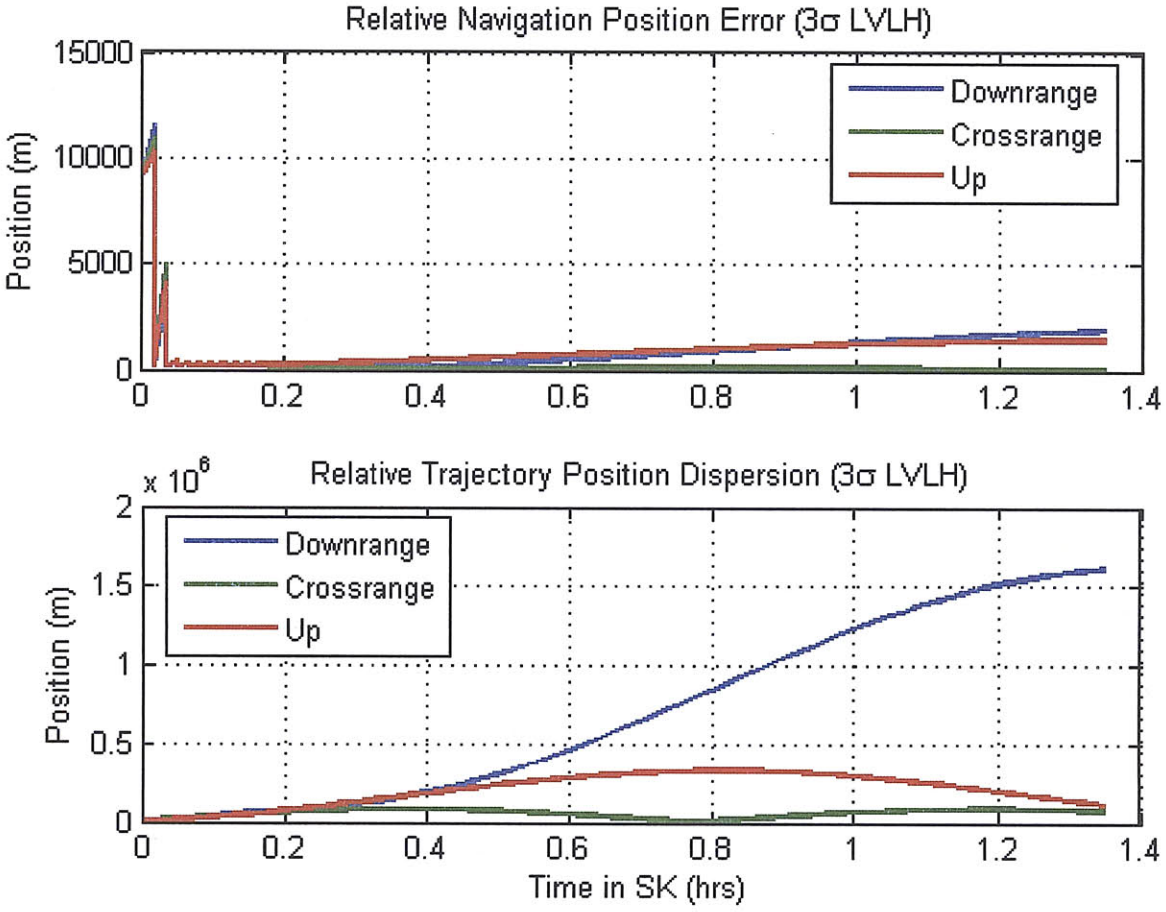

Figure B-3: Phase 2 Position Relative Navigation Dispersion, 3.0 deg/hr IMU

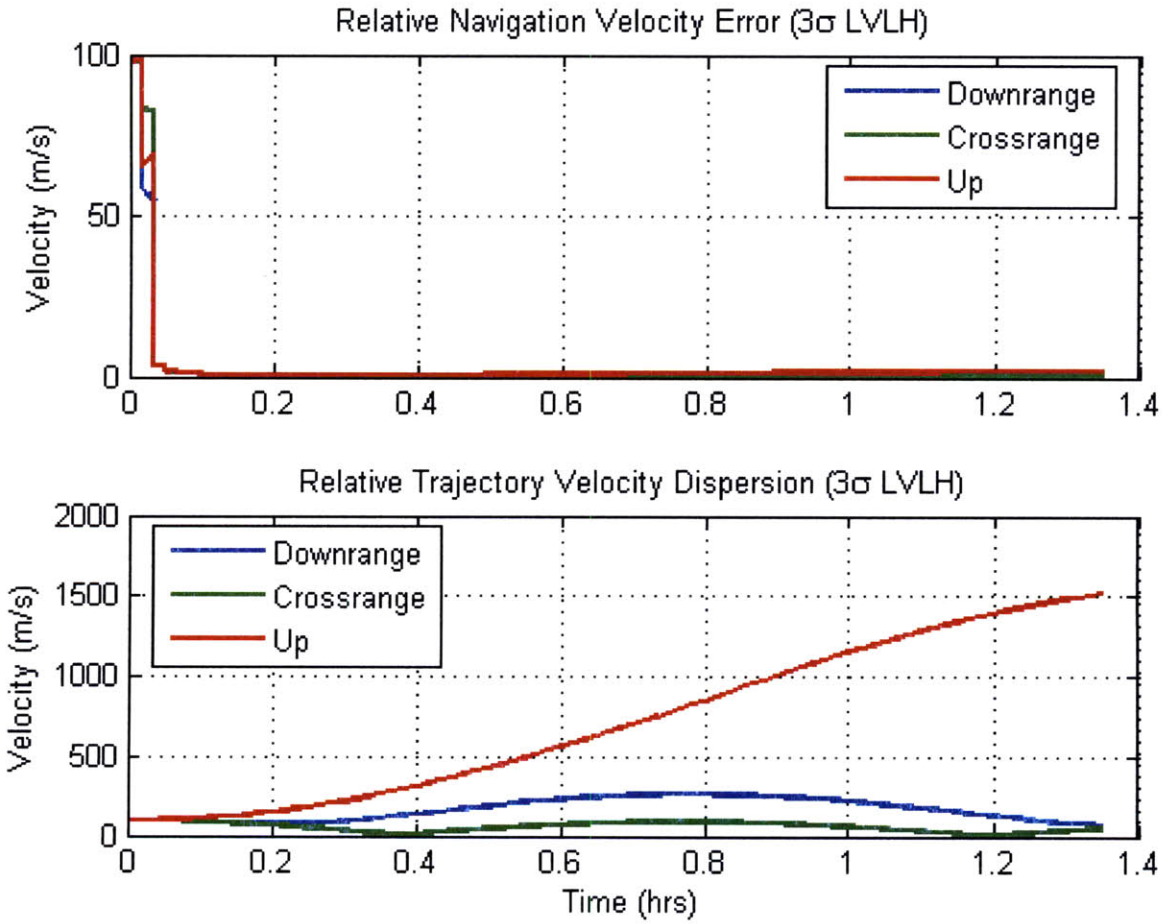

Figure B-4: Phase 2 Velocity Relative Navigation Dispersion, 3.0 deg/hr IMU

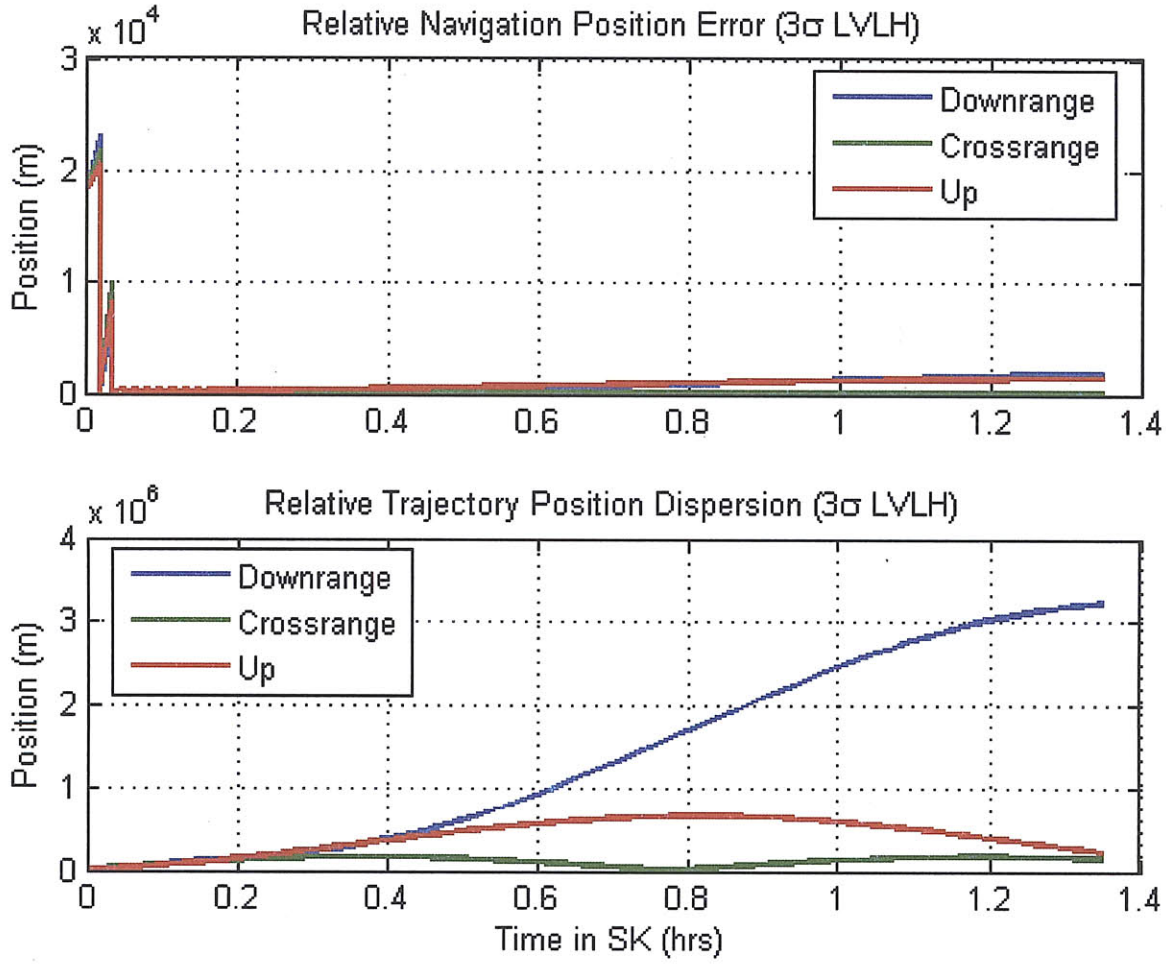

Figure B-5: Phase 2 Position Relative Navigation Dispersion, 6.0 deg/hr IMU

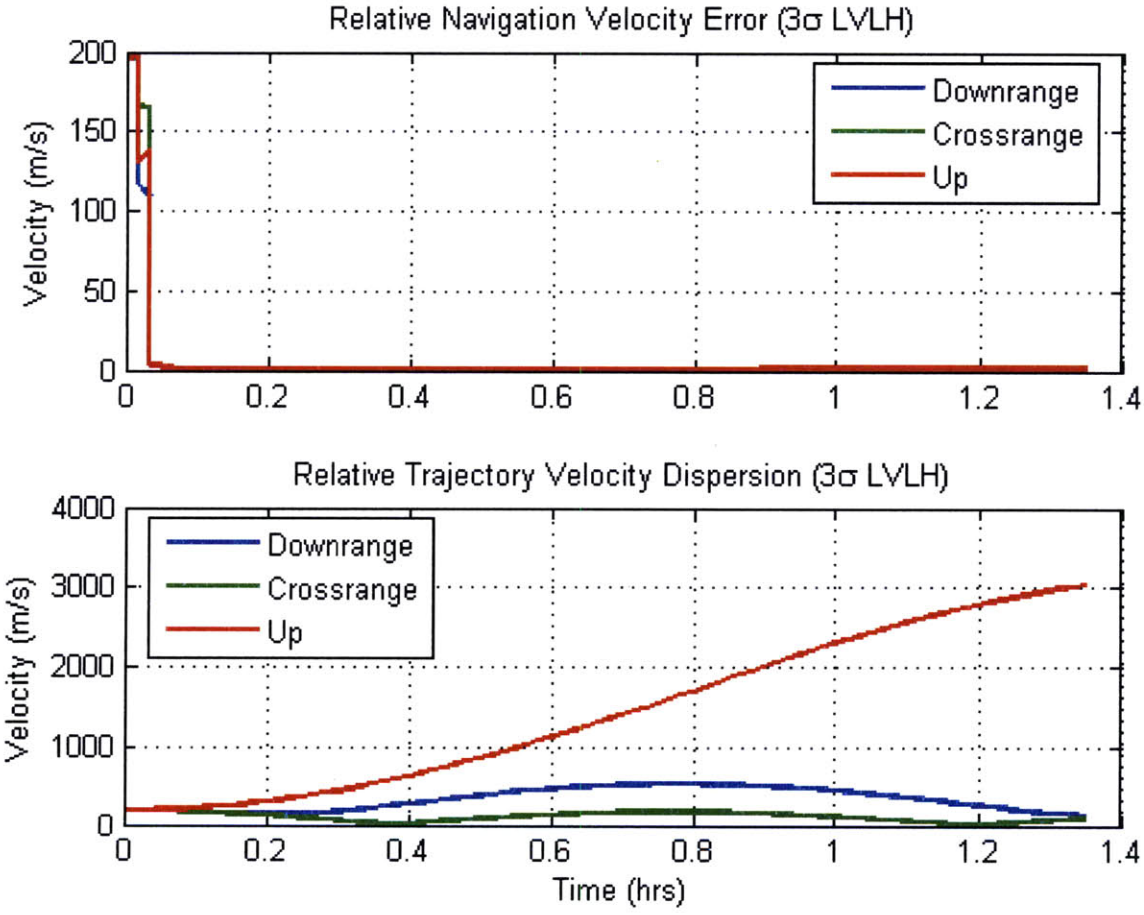

Figure B-6: Phase 2 Velocity Relative Navigation Dispersion, 6.0 deg/hr IMU

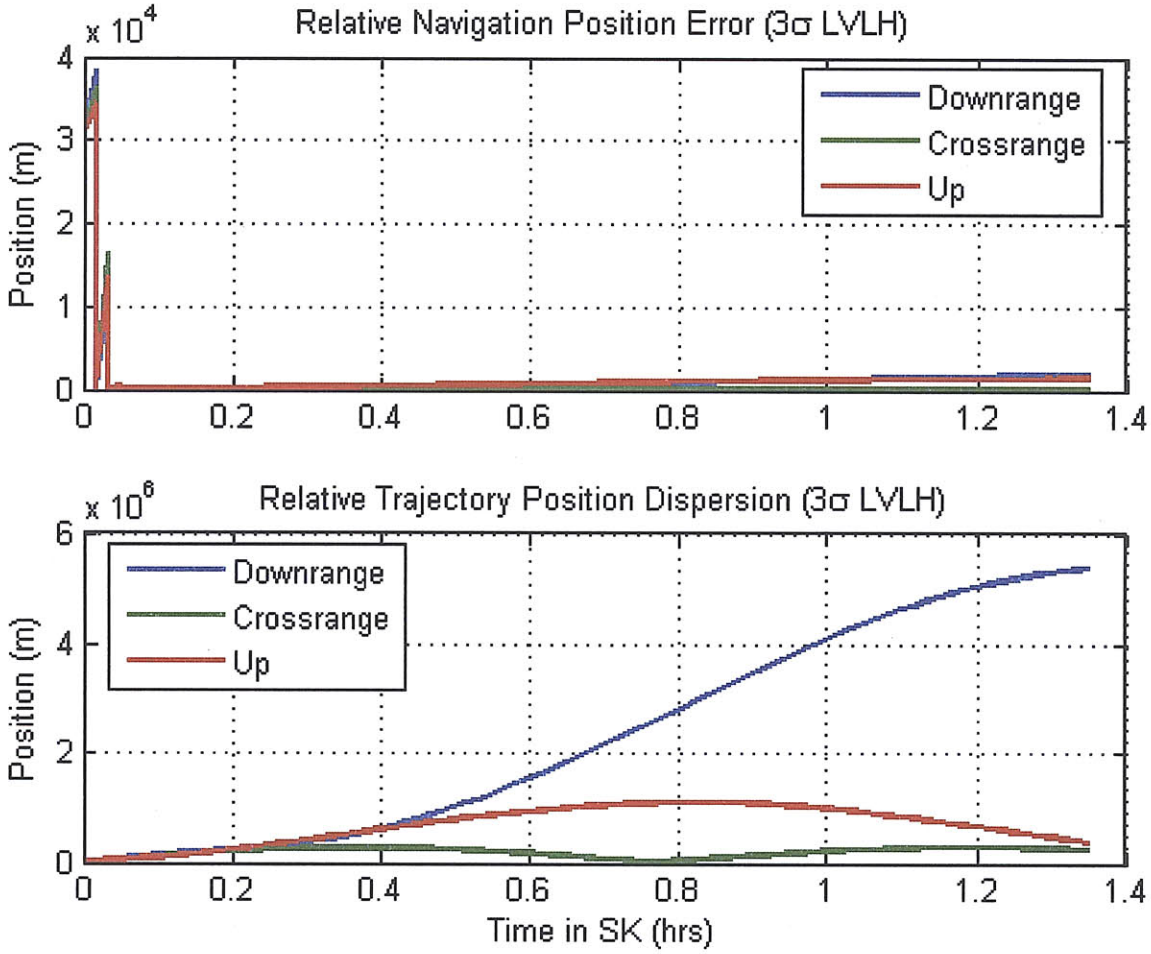

Figure B-7: Phase 2 Position Relative Navigation Dispersion, 10.0 deg/hr IMU

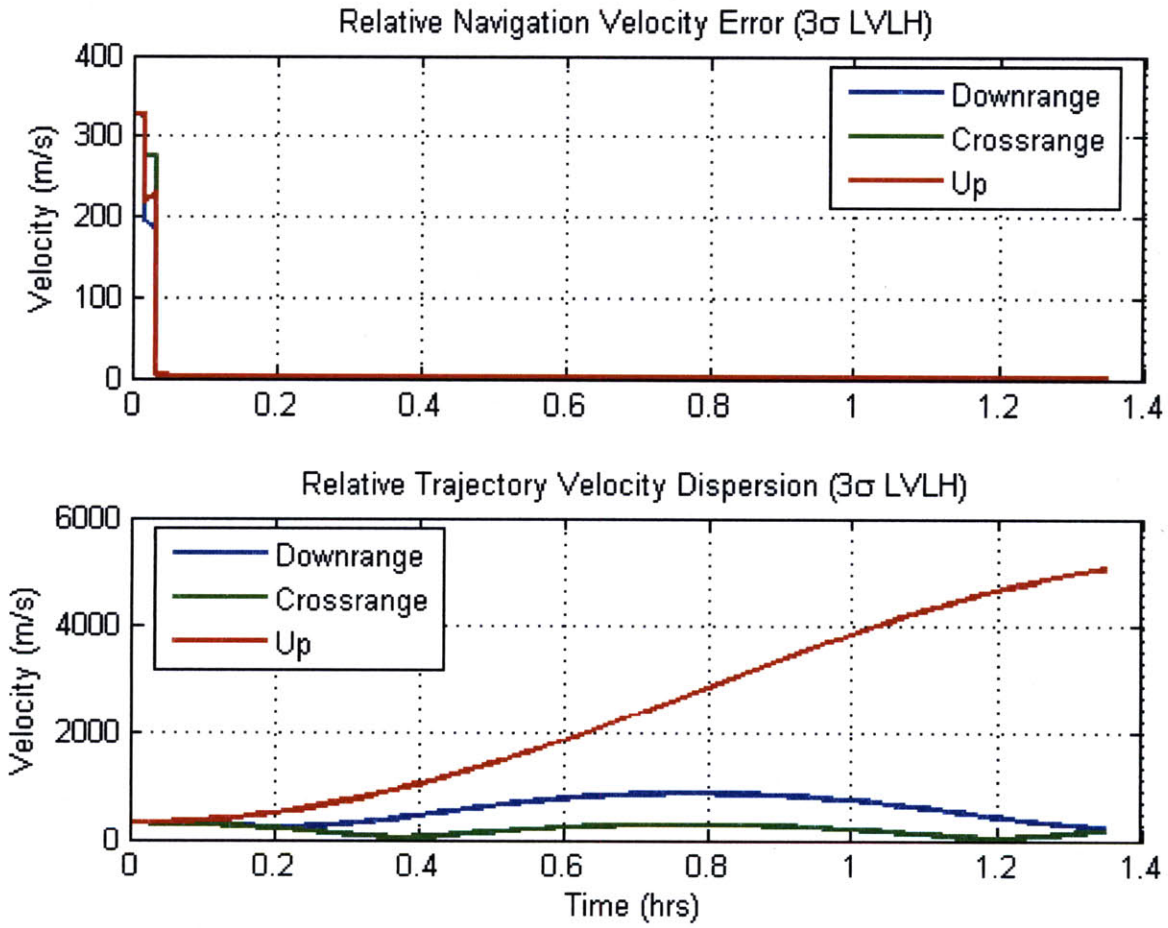

Figure B-8: Phase 2 Velocity Relative Navigation Dispersion, 10.0 deg/hr IMU

[This page intentionally left blank.]

Bibliography

[1] 30th Space Wing, United States Air Force, EELV Fact Sheet. Available at URL: http://www.vandenberg.af.mil/library/factsheets/factsheet.asp?id=5207

[2] Geller, David K. "Linear Covariance Techniques for Orbital Rendezvous Analysis and Autonomous Onboard Mission Planning," AIAA 2005-5856, Guidance, Navigation, and Control Conference and Exhibit, 15-18 Aug 2005, San Francisco, California.

[3] Battin, Richard H. *An Introduction to the Mathematics and Methods of Astrodynamics*, New York, New York: American Institute of Aeronautics and Astronautics, 1987.

[4] Sellers, J.J. *Understanding Space: An Introduction to Astronautics*, New York: McGraw-Hill, Inc., 1994.

[5] Vallado, David A. *Fundamentals of Astrodynamics and Applications*, New York: McGraw-Hill, Inc., 1997.

[6] Wertz, James R. and Wiley J. Larson. *Space Mission Analysis and Design*, El Sugundo, CA: Microcosm Press, 1999.

[7] Zimpfer, Douglas, Kachmar, Peter, and Seamus Tuohy. "Autonomous Rendezvous, Capture, and In-Space Assembly: Past, Present, and Future," AIAA 2005-2523, 1st Space Exploration Conference, 30 Jan - 1 Feb 2005, Orlando, Florida.

[8] Schmidt, George, et al. *Basic Guide to Advanced Navigation*, NATO Publication SET-054/RTG-30, 2004.

[9] Osenar, Michael J. "Performance of Automated Feature Tracking Cameras for Lunar Navigation," M.S. Thesis, Rice University, 2007, Houston, Texas.